Evaluation of easterly wave disturbances over the tropical South Atlantic in CMIP6 models

Article

Accepted Version

Cavalcante, L. C. V., Gomes, H. B., Hodges, K. ORCID: https://orcid.org/0000-0003-0894-229X, Ray, P., Herdies, D. L., Barbosa, H. M. J., Gonçalves, W. A., Silva, M. C. L., de Brito, J. I. B., Nobre, J. P. G., Lyra, M. J. A. and Baltaci, H. (2025) Evaluation of easterly wave disturbances over the tropical South Atlantic in CMIP6 models. Climate Dynamics, 63 (1). 63. ISSN 0930-7575 doi: 10.1007/s00382-024-07507-5 Available at https://centaur.reading.ac.uk/116252/

To link to this article DOI: http://dx.doi.org/10.1007/s00382-024-07507-5

Publisher: Springer

Evaluation of easterly wave disturbances over the tropical South Atlantic in CMIP6 models

Lucas C. V. Cavalcante[1], Helber B. Gomes[2], Kevin Hodges[3], Pallav Ray[4], Dirceu L. Herdies[5], Henrique M. J. Barbosa[6], Weber A. Gonçalves[7], Maria Cristina L. Silva[2], José Ivaldo B. de Brito[1], João Pedro G. Nobre[5], Matheus J. A. Lyra[2] and Hakki Baltaci[8]

[1] Academic Unit of Atmospheric Sciences, Federal University of Campina Grande, Campina Grande, Brazil

[2] Institute of Atmospheric Sciences, Federal University of Alagoas, Maceió, Brazil

[3] Department of Meteorology, University of Reading, Reading, UK

[4] Meteorology, Florida Institute of Technology, FL, USA

[5] National Institute for Space Research, Cachoeira Paulista, Brazil

[6] Physics Department, University of Maryland Baltimore County, Maryland, USA

[7] Department of Climate and Atmospheric Sciences, Federal University of Rio Grande do Norte, Natal, Brazil

[8] Institute of Earth and Marine Sciences, Gebze Technical University, Gebze, Turkey

Abstract

This study assesses the performance of the latest phase of Coupled Model Intercomparison Project (CMIP6) models in simulating easterly wave disturbances (EWD) over the tropical South Atlantic (TSA) impacting northeast Brazil (NEB). Initially, we evaluate simulated precipitation from 17 historical CMIP, 16 AMIP, 7 hist-1950, and 10 highresSST-present models against the Global Precipitation Climatology Project (GPCP) dataset to identify models that accurately reproduce the spatial and temporal precipitation patterns in the study region. The ensemble's spatial analysis demonstrates their capability in reproducing annual and seasonal precipitation climatology. However, models underestimate precipitation intensity along NEB's coast while overestimating it in TSA and NEB's north. Model uncertainties tend to be greater with higher latitudes. The models represented the annual cycle in all subareas within the study region, particularly from July to October, albeit with a greater spread in the first half of the year, especially over the Intertropical Convergence Zone (ITCZ). Based on it, three top-performing models from each ensemble were selected for EWD evaluation. The automatic tracking algorithm for EWDs showed the model's ability to represent mean values of EWD lifetime (~6 days) and phase speed (~7 m s-1) as found in ERA5 reanalysis. However, they failed to capture EWD's interannual variability or climatological mean frequency. Despite CMIP6 model weaknesses, they accurately identified two primary EWD genesis regions: one over the TSA and another near the West African coast. Overall, CMIP6 models, particularly atmospheric and high-resolution models (HighResMIP), effectively captured precipitation climatology and EWD characteristics over NEB and the adjacent TSA.

1 Introduction

Northeast Brazil (NEB), encompassing the states of Alagoas (AL), Sergipe (SE), and the eastern Bahia (BA), Pernambuco (PE), Paraíba (PB), and Rio Grande do Norte (RN), comprises ~18% of Brazil's territory and is home to ~60 million inhabitants. In recent years, the region has witnessed significant investments in the industrial and agro-industrial sectors, establishing it as the third-largest economy in Brazil, following the Southeast and South regions. Due to its vast expanse and diverse physical characteristics, NEB can be divided into sub-regions with distinct climates and precipitation regimes. Oliveira et al. (2017) identified five such sub-regions based on rainfall characteristics: north coast, south coast, north semiarid, south semiarid, and northwest. The lowest total annual precipitation occurs in the north (654.09 mm year^{-1}) and south (810.42 mm year^{-1}) semiarid regions, while the north coast and northwest NEB regions experience the highest annual precipitation (1450 mm year^{-1}). Rodrigues et al. (2020) observed distinct rainy seasons across NEB, with precipitation occurring between February and May in the north, April and July on the north coast, and December and March in the south and semiarid coast.

The spatial and temporal variability of rainfall regimes in NEB is influenced by a myriad of global, synoptic and regional-scale processes. At the synoptic scale, various processes influence the NEB's precipitation regime. These include the penetration of cold fronts or their remnants between latitudes 5°S and 18°S (Kousky 1979; Molion and Bernardo 2002), the Intertropical Convergence Zone (ITCZ) (Hastenrath and Heller 1977; Nobre 1993; Nobre and Shukla 1996; Melo 2009), Upper-Tropospheric Cyclonic Vortices (UTCV) (Kousky and Gan 1981; Gan and Kousky 1986; Alves 2001; Oliveira et al. 2017; Dos Reis et al. 2021), Mid-Tropospheric Cyclonic Vortices (Fedorova et al. 2016), and Easterly Wave Disturbances (EWD) (Neiva 1975; Yamazaki and Rao 1977; Ferreira et al. 1990; Pontes da Silva 2011; Gomes et al. 2015; Gomes et al. 2019). For example, Oliveira et al. (2017) emphasize the importance of UTCV and the South Atlantic Convergence Zone (SACZ) in shaping NEB's precipitation regime, highlighting mechanisms that lead to dry periods in the south coasts and rainy periods in the north coasts.

EWDs are transient synoptic-scale disturbances, propagating from east to west in the trade wind region, that significantly contribute to NEB's precipitation, with over half of the total annual precipitation in the eastern NEB is associated with these systems (Gomes et al. 2019). These disturbances as evidenced by those two recent extreme precipitation events in east coast of NEB during 2022 and 2023 (Lyra et al. 2024; Freitas 2022; Portela 2022). EWD activity can be observed in all tropical ocean basins with peaked between latitudes of 10-15° in both hemispheres during warmer months (Hollis et al. 2023). Its frequency also varies across regions and atmospheric levels, notably at 700 hPa (South Atlantic Ocean, South Pacific Ocean) or 850 hPa (central North Pacific Ocean, South Indian Ocean), with 700 hPa showing higher activity (Hollis et al. 2023). While studies on EWDs in the Southern Hemisphere (SH) are limited compared to the NH, recent efforts have been made to characterize these systems, particularly in the Tropical South Atlantic (TSA) basin close to the Brazilian coast. However, challenges arise from the variability in EWD structure and characteristics, influenced by their propagation within zonal currents and seasonal variations (Asnani 1993). Different identification methods and study periods used in previous research have resulted in discrepancies in the observed characteristics of EWDs, albeit with some notable similarities (Table 1).

Table 1 Characteristics of EWDs over the Tropical South Atlantic Basin according to referenced studies.

For identifying and tracking EWDs in this region, Gomes et al. (2015) used an automated method, called TRACK, based on Hodges (1995, 1999), who developed it for tracking EWDs on the East African coast (Hopsch et al.

2007; Serra et al. 2010; Thorncroft and Hodges 2001). Applying this tracking method on 21 years (1989-2009) of European Centers for Medium-Range Weather Forecasting interim reanalysis (ERAI) data, Gomes et al. (2019) successfully tracked 342 EWDs out of 518 manually detected EWDs in the TSA, a success rate of 66%. The majority of the untracked EWDs formed very close to the coast of the continent and were filtered out due to the selection criteria. Gomes et al. (2019) observed that 97% of the EWDs reached the NEB coast during their evolution, 64% showed significant convective characteristics and 14% reached the Amazon region. The highest frequency of EWDs was found between April and August (rainy season), with 429 cases identified, which accounted for 60% of the total precipitation from the coast of Alagoas to the east of Paraíba. The other months presented less than half of the cases, where the periods with the lowest frequency are between October and December, and are more frequent in La Niña years, especially in years with stronger or longer-lasting ENSO episodes. Regarding the genesis of EWDs, the authors identified five associated systems. The main contributor is frontal remnants that propagate at low latitudes, accountig for 72.20% of cases. Convective clusters of the west coast of Africa contribute to 10.04% cases, followed by the ITCZ at 6.37%, and UTCV at 1.54%.

To explore these complex characteristics of the EWDs, numerical models have become indispensable. In particular, the Coupled Model Intercomparison Project (CMIP) models (Eyring et al. 2016) have been instrumental across different regions of the globe (e.g., Dong and Dong 2021; Ngoma et al. 2021; Shiru and Chung 2021; Babaousmail et al. 2021). Studies evaluating CMIP6 model performance over South America reveal mixed results, with challenges in accurately reproducing precipitation characteristics (e.g., Rivera and Arnould 2020; Ortega et al. 2021), particularly during monsoon seasons (Dias et al. 2021). While some models excel the results of Firpo et al. (2022) showed better model performance in reproducing spatial patterns of winter (JJA) precipitation, others struggle, especially in regions like NEB (Firpo et al. 2022). Model limitations in simulating cloud physics and the Low-Level Jet Stream contribute to discrepancies in summer precipitation estimates, with underestimations in the Amazon region and overestimations in NEB (Reboita et al. 2010; Firpo et al. 2022). Despite these challenges, models generally captured the annual cycle of precipitation over NEB, albeit with some overestimations during wet months.

Further evaluations across various CMIP model generations (CMIP3, CMIP5, and CMIP6) underscores deficiencies in representing precipitation and climate extremes in tropical SA (Medeiros et al. 2022). Model performance varied depending on the specific index investigated and the macro-region of Brazil under consideration, with pronounced uncertainties in the north and northeast, and lower uncertainties in the south and southeast. Although no single model emerged as superior, CMIP6 models exhibited better performance over north, southeast, and south regions compared to earlier versions. However, challenges persists in accurately simulating key meteorological features that characterize the climate in various regions of South America, such as the ITCZ, Subtropical and polar jet streams, Bolivian High, and the NEB trough (Bazzanela et al. 2023), particularly in summer months. Common characteristics observed across all models include superior performance in winter, a double trend of the ITCZ in both summer and winter, underestimation of precipitation in northern Brazil, and overestimation on the west coast of South America and NEB during summer.

Understanding how climate models simulate observed historical climate provides useful information about their reliability in projecting future climate change. Hence, this study aims to evaluate the CMIP6 models' ability to capture the characteristics of EWDs over the TSA during peak activity period (April to August) in the current climate. Through comprehensive evaluation and comparison with observational data, this study seeks to contribute to better understanding of model performance and its implications for future climate projections. The rest of the paper is organized as follows: Section 2 describes data and methods, Section 3 discusses results, followed by conclusions in Section 4.

2 Material and methods

The choice of the study area (Fig. 1; 5°N-20°S and 0°-60°W) was driven by our objective to capture the nuanced variations in precipitation patterns within the NEB and the adjacent TSA. The study area encompasses most of the Brazilian territory, including the entire NEB and parts of the Brazilian north and southeast regions, and the TSA covering the entire coastline of the NEB extending toward the West African coast. To better represent the different precipitation regimes within the NEB and the variety of meteorological systems that influence this region, the total area was divided into 8 subareas: area 1 (5-15°S and 45-40°W) represents the semiarid region; area 2 (5-15°S and 40-35°W) represents the NEB coast; areas 3 (5-15°S and 35-30°W) and 4 (5-15°S and 30-25°W) represent the path of EWDs until they reach the NEB; and areas 5.1 (5°N-0° and 35-20°W), 5.2 (0-5°S and 35-20°W), 6.1 (5°N-0° and 20-5°W), and 6.2 (0-5°S and 20-5°W) represent the ITCZ region, divided to better represent its seasonal displacement.

Fig. 1 The study area (5°N-20°S and 0°-60°W) and its 8 subareas: 1 (5-15°S and 45-40°W) represents the semiarid region; area 2 (5-15°S and 40-35°W) represents the NEB coast; 3 (5-15°S and 35-30°W) 4 (5-15°S and 30-25°W) represent the path of EWDs until they reach the NEB; and 5.1 (5°N-0° and 35-20°W), 5.2 (0-5°S and 35-20°W), 6.1 (5°N-0° and 20-5°W), and 6.2 (0-5°S and 20-5°W) represent the ITCZ region.

In CMIP phase 6, substantial updates were introduced compared to the prior phase (Eyring et al. 2016). Notably, this phase includes the CMIP's historical simulations and the Diagnostic, Assessment, and Characterization of Klima (DECK) framework, which contains the Atmospheric Model Intercomparison Project (AMIP) historical simulations. This aims to ensure model continuity and preserve fundamental characteristics across CMIP phases. An innovative addition in this phase is the endorsed Model Intercomparison Projects (MIP), specifically designed to address targeted questions and bridge scientific gaps from earlier CMIP phases.

Outputs from AMIP models and CMIP's historical simulations were utilized at the highest available spatial resolution (Table 2). Model selection was contingent upon the presence of the first ensemble member (r1i1p1f1) within the specified analysis scope. Given the relatively small scale of EWDs compared to other synoptic-scale systems, the High-Resolution Model Intercomparison Project (HighResMIP) was employed with increased horizontal resolutions of approximately 50 km or 25 km in both the atmosphere and ocean (Haarsma et al., 2016). Specifically, outputs from coupled models (hist-1950) and atmospheric models (highresSST-present) from the first level of HighResMIP were considered for this study.

Table 2 Description of the CMIP6 models used in this study.

Precipitation estimates from the Global Precipitation Climatology Project Version 3.1 (GPCP; 0.5° x 0.5°; Huffman et al. 2020; Bazzanela et al. 2023) were used to evaluate model performance. Developed under the auspices of the World Climate Research Program (WRCP), GPCP provides global monthly precipitation estimates by combining rain gauge stations, satellite data, and sounding observations. The GPCP dataset is available from 1983. The assessment of model performance was conducted over the common period of 1983-2014, during which both GPCP and model outputs are available. For consistent comparisons, all data were interpolated to a uniform 1° x 1° grid resolution.

2.1 Statistical analysis

The robustness of precipitation from each CMIP6 model and their ensembles at both annual and seasonal (April to August) time scales are assessed by comparing them to GPCP. The ensembles comprise the mean of all models within each model set (CMIP, AMIP, hist-1950, and highresSST-present). Climatological annual and seasonal averages were computed from monthly data.

For evaluating the coherence of CMIP6 model ensembles against GPCP over the entire study area (Fig. 1), we use various statistical measures, such as Arithmetic Mean (Eq. 1), Mean Bias (Eq. 2), and Spread (Eq. 3). These parameters represent precipitation values from individual models (Pp), ensembles (Ep), and GPCP (Op) at each grid point (n) within the total domain presented in Figure 1.

$$MEAN = \frac{1}{n}\sum_{t=1}^{n}\left(E_p\right) \quad (1)$$

$$BIAS = \frac{\sum_{p=1}^{n} E_p}{n} - \frac{\sum_{p=1}^{n} O_p}{n} \quad (2)$$

$$SPREAD = \sqrt{\frac{1}{n}\sum_{p=1}^{n}\left(P_p - E_p\right)^2} \quad (3)$$

For evaluating model performance over subareas for annual precipitation variability, Box Plots (Tukey 1977) were constructed. The calculations utilized outputs from CMIP, AMIP, hist-1950 and highresSST-present models across all eight subareas.

For evaluating performance of individual models, we use Taylor diagrams (Taylor 2001), whose parameters include Pearson correlation (R^2; Eq. 4) between simulated (Pi) and observed (Oi) precipitation and the model's normalized standard deviation (Eq. 5). Annual mean precipitation values in each of the eight subareas were employed for this analysis. Additionally, to create a ranking based on the model's performance, other parameters such as Root Mean Square Error (RMSE; Eq. 6) and Taylor Skill Score (TSS; Eq. 7) were utilized. Here, R^2 (Eq. 4) denotes the correlation coefficient of the spatial pattern between model outputs and observations, R^2L is the highest achievable value (set to 1), and σP and σO are the simulated and observed standard deviations, respectively

$$R^2 = \frac{\sum_{i=1}^{n}(P_i-\underline{P}_i)(O_i-\underline{O}_i)}{\sqrt{\sum_{i=1}^{n}(P_i-\underline{P}_i)^2}\sqrt{\sum_{i=1}^{n}(O_i-\underline{O}_i)^2}} \quad (4)$$

$$\sigma_N = \frac{\sigma_P}{\sigma_O} \quad (5)$$

$$RMSE = \sqrt[2]{\frac{1}{n}\sum_{i=1}^{n}(P_i - O_i)^2} \quad (6)$$

$$TSS = \frac{4(1+R^2)^2}{\left(\frac{\sigma_P}{\sigma_O}+\frac{\sigma_O}{\sigma_P}\right)^2(1+R^2{}_L)^2} \quad (7)$$

2.2 Automatic tracking algorithm

An automatic tracking algorithm was applied to models that exhibited superior performance in the previous stage. Data were obtained for zonal and meridional winds at 6-hour intervals from 1989 to 2009 - the period corresponding to the climatology proposed by Gomes et al. (2019). The number of vertical levels varied among models, with the majority providing data for levels at 850, 500, and 250 hPa, while some models also included levels at 925, 700, 600, and 50 hPa. In addition to the Gomes et al. (2019) study, a TRACK run using the European Centers for Medium-Range Weather Forecasting reanalysis version 5 (ERA5) was also used to evaluate model performance.

For identifying the EWDs in the CMIP6 models, we used the automatic identification and tracking method TRACK (Hodges 1995, 1999). This method identifies and tracks EWDs based on the minimum of relative vorticity in the southern hemisphere, which signifies cyclonic systems, adhering to specific criteria concerning their lifetime and distance traveled. Given the distinct characteristics of EWDs in the TSA and TNA, including their intensity and distance traveled (Asnani 1993), adjustments were made to the tracking algorithm to enable the identification of systems along the TSA that reach the NEB coast. Thus, the identification and tracking criteria used here are the same as those in Gomes et al. (2015, 2019). The main changes include applying the tracking algorithm at a higher resolution, from T42 (~310 km) to T63 (~210 km), reducing the minimum distance traveled by EWDs to 500 km (~5°), requiring a persistence of at least 1.5 days, and setting the minimum threshold of relative vorticity to -0.5 x 10^{-5} s^{-1} or lower. The algorithm was applied at the 850 hPa level, where the centers of relative vorticity are more intense and better identified.

3 Results and discussions

3.1 Climatology of ensembles and their spread

The climatological characteristics and variability of precipitation among different ensemble simulations are examined in this section. Figure 2 shows the annual (left column) and seasonal climatology (right column) of precipitation for the CMIP (Fig. 2b, g), AMIP (Fig. 2c, h), hist-1950 (Fig. 2d, i), and highresSST-present (Fig. 2e, j) ensembles, as well as for GPCP observations (Fig. 7a, f). GPCP data show regions of low precipitation over the TSA that are associated with the Subtropical High, and areas with heavy precipitation exceeding 4 mm day^{-1} that are associated with the ITCZ and northern Brazil. For April to August (AMJJA), minimal precipitation is observed over the São Francisco basin (Fig. 2f) across all ensembles, with highresSST-present best representing their spatial extent (Fig. 2e). Moreover, regions along the NEB coasts exhibit precipitation exceeding 3 mm day^{-1}, indicative of the EDWs activity, consistent with previous studies (Gomes et al., 2019). The The GPCP annual climatology (Fig. 2a) exhibits two precipitation nuclei, one in the northern coast and the other in the southern coast, while the seasonal climatology (Fig. 2f) reveals a broader area of precipitation exceeding 4 mm day^{-1} covering the entire eastern NEB. The AMIP ensemble best represented both areas of high precipitation (Fig. 2c, h), while ensembles with higher resolution (HighResMIP) faced difficulties in reproducing these features, especially hist-1950 (Fig. 2d, i). Although large-scale spatial patterns were captured in all ensembles, limitations are observed in precipitation intensity, especially along the NEB coast and the ITCZ. Among the ensembles, CMIP showed the greatest differences in both intensity and positioning of observed precipitation patterns.

Fig. 2 Annual (left column) and seasonal (right column, April to August or AMJJA) average precipitation (mm day^{-1}) from the GPCP (a, f), CMIP (b, g), AMIP (c, h), hist-1950 (d, i), and highresSST-present (e, j) model ensembles during the period of 1983-2014.

Figure 3 illustrates the annual (left column) and seasonal bias (right column) in precipitation among the ensembles for CMIP (Fig. 3a, e), AMIP (Fig. 3b, f), hist-1950 (Fig. 3c, g), and highresSST-present (Fig. 3d, h). All ensembles overestimated precipitation in the northern NEB and the adjacent latitudinal band of the TSA, with the CMIP ensemble displaying the most pronounced bias of +2.5 mm day^{-1} for the annual mean (Fig. 3a) and +3 mm day^{-1} for the seasonal mean (Fig. 3e) over the adjacent TSA. On the other hand, low bias is evident in the HighResMIP (Fig. 3c, d, g, h) in this same region. In all cases, precipitation was underestimated over the NEB coast, especially during the peak activity of the EWDs. The highest bias in this region was found in the high-resolution models (Fig. 3g, h). This bias is also evident, albeit to a lesser extent, in the HighResMIP (Fig. 3c, d), CMIP (Fig. 3a) and AMIP (Fig. 3b), particularly in the coastal areas of Bahia. The HighResMIP ensemble showed biases close to 0 mm day^{-1} over the semi-arid region of the NEB (Fig. 3c, d), corroborating with their better representation of the subsidence region over the São Francisco basin (Fig. 2f). Additionally, part of the northern Brazil showed lower precipitation in all ensembles. Overall, deviations were more pronounced in the seasonal climatology and in the CMIP ensembles (Fig. 3a, e).

Fig. 3 Bias for annual (left column) and seasonal (right column) mean precipitation (mm day^{-1}) for the CMIP (a,e), AMIP (b,f), hist-1950 (c,g), and highresSST-present (d,h) model ensembles during the period of 1983-2014. The dashed line corresponds to the Bias values.

The spatial distribution of the spread between the ensemble members (Fig. 4) shows greater uncertainty at latitudes farther north and decreasing toward southern latitudes, particularly close to the ITCZ. Using a spread line equal to 1 mm day^{-1} as a threshold, it becomes apparent that for CMIP, this line is near 15°S over the continent and 10°S over the TSA for the annual mean (Fig. 4a), while for the seasonal mean (Fig. 4e), this line is close to 8°S on the continent and 12°S on the TSA. This feature is observed in all ensembles and is more pronounced in hist-1950, where the line is located near 20°S over the continent and 5°S on the TSA for the annual mean (Fig. 4c). Thus, the decrease is more pronounced over land compared to the TSA, especially in the annual mean. The spread in the seasonal mean of the HighResMIP shows the lowest uncertainty over the continent, especially in hist-1950, where a region with values less than or equal to 0.25 mm day^{-1} is observed over the São Francisco basin (Fig. 4g). In the seasonal maps (Fig. 4; right column), the NEB coast stands out as a region with higher uncertainty compared to the surrounding areas, especially in the CMIP (Fig. 4e) and AMIP (Fig. 4f) ensembles.

Fig. 4 The annual (left column) and seasonal (right column) precipitation spread (mm day^{-1}) for the CMIP (a, e), AMIP (b, f), hist-1950 (c, g), and highresSST-present (d, h) during the period of 1983-2014. The dashed line corresponds to the annual and seasonal climatological average of precipitation.

3.2 Annual Cycle

Figure 5 shows the annual cycle of precipitation in each subarea (Fig. 1) for CMIP models (green box), AMIP (red box), hist-1950 (gray box), and highresSST-present (blue box), along with GPCP data as a reference (dotted black line). All model sets successfully capture the annual precipitation cycle in all subareas. The model ensembles exhibit greater spread in the first half of the year (January to June). During this period, the largest discrepancies compared to GPCP data were observed, with overestimation of precipitation in all areas except for subareas 5.1 and 6.1, where underestimation occurred.

The uncertainty and discrepancy against GPCP data were more pronounced in subareas corresponding to the ITCZ (5.1, 5.2, 6.1, and 6.2), especially in the northern part (5.1 and 6.1), and in the CMIP models. In other subareas, the models showed greater proximity to the GPCP, especially between July and October, extending into December in subareas 2, 3, and 4, and from May to October in subarea 1. The AMIP and HighResMIP models exhibited similar patterns, which significantly differed from the CMIP models. Nonetheless, the hist-1950 models significantly deviated from these patterns from April to June in areas 1, 2, 3, and 5.2 (Fig. 5a, b, c, f).

Fig. 5 Annual cycle of model and observation for the 8 subareas as depicted in Fig. 1. The green (CMIP), red (AMIP), gray (hist-1950), and blue (hishresSST-present) box plots represent the distribution of monthly precipitation for all members in areas: 1(a), 2(b), 3(c), 4(d) , 5.1(e), 5.2(f), 6.1(g) and 6.2(h). The black line overlaid on the diagram represents the annual precipitation variability of GPCP and the open circles are the outliers.

3.3 Individual Model Analysis

Fig. 6 Taylor diagram for the annual mean precipitation in the 8 subareas (as shown in figure 1). The normalized standard deviation is shown on the x-axis and y-axis, and the correlation coefficient is shown on the curved side.

The performance of individual models for annual mean precipitation across 8 subareas is shown in Taylor diagrams for CMIP (Fig. 11a), AMIP (Fig. 11b), hist-1950 (Fig. 11c), and highresSST-present (Fig. 11d) models. CMIP, AMIP, hist-1950, and highresSST-present models exhibit normalized standard deviation (correlation) values between 0.57-6.99 mm day^{-1} (0.001-0.987), 0.37-3.35 mm day^{-1} (0.28-0.990), 0.14-4.52 mm day^{-1} (0.018-0.96), and 0.73-2.26 mm day^{-1} (0.398-0.993), respectively. Same coupled models within CMIP, exhibited correlation values close to 0, such as MPI-ESM1-2-HR (0.001) and EC-Earth3-Veg (0.009), as well as BCC-CSM2-MR (0.018) from hist-1950. HighresSST-present models showed the highest correlations, with HadGEM3-GC31-HH from hist-1950 being the only model with a correlation exceeding 0.90 in area 5.1. Among CMIP, AMIP, and highresSST-present models, area 6.2 exhibited the highest correlations, followed by 5.2 and 1, while area 5.1 showed the lowest values in AMIP and highresSST-present models. Thus, better model performance is observed in the south of the ITCZ, the semi-arid region, and the NEB coast compared to the north of the ITCZ and adjacent ATS. For hist-1950 models, the highest correlations are found in area 1, followed by areas 6.1 and 5.2, with the lowest correlation observed in area 3, indicating better performance in the semi-arid and ITCZ than the adjacent ATS. Regarding the normalized standard deviation, highresSST-present models show values closest to the reference (1), while CMIP models are the farthest away. In CMIP, AMIP, and highresSST-present models, values in areas 5.1 and 6.1 (north of the ITCZ) are closest to 1 mm day^{-1}, while the farthest are in areas 4 and 2 (NEB's coast and ATS). This suggests that although models may exhibit high correlation in certain areas, they also show greater dispersion of annual means compared to GPCP in those same areas.

Despite some models performing well in certain regions and poorly in others, consistency across all areas was considered in selecting the best models. Noteworthy models include ECMWF-IFS-HR and MRI-AGCM3-2-H from highresSST-present, along with ECMWF-IFS-LR and CMCC-CM2-VHR4. ECMWF-IFS-HR exhibited correlation exceeding 0.92 in all areas except for area 3 (0.88), outperforming its lower-resolution counterpart. ECMWF-IFS-LR, which showed values over 0.90 except for areas 3 (0.83) and 5.1 (0.86), with both models having similar average standard deviations: 1.100 mm day^{-1} (ECMWF-IFS-HR) and 1.108 mm day^{-1} (ECMWF-IFS-LR). CMCC-CM2-VHR4 achieved values exceeding 0.90, except for area 5.1 (0.71). MRI-AGCM3-2-H exhibited correlations exceeding 0.92, except for areas 2 (0.80), 3 (0.71), and 4 (0.85), with standard deviations between 1.103 and 1.270 mm day^{-1}. Among the AMIP models, CMCC-CM2-SR5 stood out with a correlation exceeding 0.92, except for area 5.1 (0.67), with standard deviations between 0.76 and 1.62. INM-CMS-0 and CAS-FGOALS-I3-L exhibited correlations exceeding 0.90 in areas 5.2 and 6.2, respectively. BCC-CSM2 from CMIP demonstrated a correlation exceeding 0.90 in area 6.2, outperforming its higher-resolution counterpart, which exhibited the lowest correlation. Despite inferior results compared to highresSST-present, ECMWF-IFS-HR and CMCC-CM2-VHR4 also performed well among hist-1950 models.

Fig. 7 Annual and seasonal values of RMSE (mm day^{-1}) (a), and annual values of R^2 and TSS (b), corresponding to the average of the 8 subareas for each model.

To select the best performing models, we examine the RMSE (Fig. 7a), TSS and Pearson correlation (Fig. 7b) for both annual and seasonal means of the eight subareas for each model, see supplementary material Table 1S for CMIP models, Table 2S for highresSST-present models, Table 3S for hist-950 models and Table 4S for AMIP models. The results indicate that the RMSE is generally lower for the annual period compared to seasonal period, with CMIP models exhibiting the highest values: 1.6-3.4 mm day^{-1} (annual) and 1.6-4.0 mm day^{-1} (seasonal). AMIP models showed closely clustered values, between 1 and 1.8 mm day^{-1}, with CAS.FGOALS-f3-L and AS-RCEC.TaiESM1 standing out from the rest. Among the HighResMIP models, 4 highresSST models had RMSE below 1 mm day^{-1}: ECMWF-IFS-HR, ECMWF-IFS-LR, CMCC-CM2-VHR4, and MRI-AGCM3-2-H, along with the ensemble. In contrast, only the HadGEM3-GC31-HH model from the hist-1950 had RMSE below 1 mm day^{-1}. The TSS index and Pearson correlation varies from 0 to 1, with values closer to 1 indicating better model performance. In CMIP models, only the NCC.NorESM2-MM model exhibits a TSS exceeding 0.6 (0.619). The four aforementioned highresSST models had TSS above 0.8 and average correlation above 0.9. The HadGEM3-GC31-HH model from hist-1950 exhibited both correlation and TSS above 0.8. Standout AMIP models were CMCC-CM2-SR5 with TSS of 0.837, and average correlation of 0.910, and AS-RCEC.TaiESM1 with 0.859 and 0.894, respectively.

Table 3 lists the top three performing models from each ensemble. CAS.FGOALS-f3-L and AS-RCEC.TaiESM1 models excelled in both CMIP and AMIP ensembles, with AMIP showing the better results overall. CMCC-CM2-SR5 was the best-performing model among AMIP models, although its CMIP version did not yield satisfactory results, having one of the lowest TSS (0.401). ECMWF-IFS-LR from highresSST showed excellent performance, ranking second best overall, but was not included in the set as its values were slightly lower than ECMWF-IFS-HR, a higher-resolution model, emphasizes the role of resolution in model performance.

Table 3 TSS (annual), RMSE (annual and seasonal), bias (annual and seasonal), R^2 (annual), and normalized standard deviation of the models with the best performance from each set, corresponding to the average of the 8 subareas for each model.

3.4 TRACK

Due to missing U and V wind components within the study period for some selected models, the analysis of EWDs was conducted on 9 out of the 12 selected models, comprising two from each model set. Only the 850 hPa level was evaluated in contrast to previous studies (GOMES et al., 2015 and 2019; HOLLIS et al., 2023) due to data limitations. For the same reason, the ensembles were not included in this analysis stage despite achieving good results.

The EWD's identified in the models showed similar characteristics to those reported by Gomes et al. (2019), with mean lifetimes ranging from 5.84 to 6.51 days and phase speeds between 6.37 and 7.07 m s^{-1}, closely aligning with ERA5 (5.78 days and 7.29 m s^{-1}). Both datasets indicated EWD lifetimes approaching the climatological value of 4 to 6 days, albeit slightly slower at 9.5 m s^{-1}. The frequency of EWDs during 1989 to 2019 showed similarities between ERA5 (27 EWD year^{-1}) and climatology (25 EWD year^{-1}). However, overall, the models overestimated the number of EWD's per year, between 41.1 and 49.5 EWDs year^{-1} in CMIP and AMIP models, with the NCC.NorESM2-MM from CMIP closest to climatology (31.1 EWDs year^{-1}). This difference is accentuated in the HighResMIP coupled and atmospheric models, which showed ~3 times more EWDs (74.7 and 78.6 EWD year^{-1}) compared to the climatological average and ERA5 (Table 4). As noted by Hollis et al. (2023), the most prominent level of EWD occurrence in the TSA is at 700 hPa. Hence, the choice to evaluate only at the

850 hPa might have resulted in increased noise, particularly in high-resolution models, with some cyclonic vorticity centers potentially not being accurately characterized as EWDs.

Table 4 EWD characteristics identified by TRACK method and the correlation between models and ERA5 and Gomes et al. (2019) of EWD interannual variability (R^2) from 1989 to 2019.

Although the differences between ERA5 (this work) and ERA-Interim (GOMES et al., 2019), we observe the same variability pattern over the years (Fig. 8). Figure 8 presents the EWD frequency from 1989 to 2009 for each model. Evaluating the interannual variations of EWD between the models and from ERA5 and the climatology of Gomes et al. (2019), a low correlation is observed in both cases, with the ECMWF-IFS-HR (highresSST-present) and AS-RCEC.TaiESM1 (highresSST-present) (AMIP) presenting the highest values (~0.35). Because of that, the CMIP6 models were unable to reproduce the interannual variation of EWDs as observed in both climatology and ERA5, making it impossible to observe variations during El Niño and La Niña years.

Fig. 8 EWD's frequency from 1989 to 2019 identified in coupled models (red bars) and atmospheric models (blue bars) for CMIP and AMIP models (a), and for hist-1950 and highresSST-present (b). The solid black dashed line represents the EWD's frequency identified by ERA5 reanalysis data, and the solid line represents the EWD's climatological frequency from Gomes et al. (2019).

Assessing the EWD's genesis locations using ERA5 (Fig. 9a), a concentration was observed between 25-15°W, with a northwest-southeast inclination and another cluster near the African coast between 5-10°E. These core positions align closely with the two main systems associated with EWD formation (Gomes et al., 2019), namely the frontal remnants propagating at low latitudes and the convective clusters off the west coast of Africa. While these cores were observed in all models, except for the HighResMIP models, additional cores were detected in other models: one positioned farther north between the aforementioned cores and another near the NEB coast (Fig. 9b-e).

Analysis of the EWD density map based on ERA5 reveals two centers of higher EWD frequency, one near the NEB coast and the other near the west coast of Africa, coinciding with the genesis regions of these systems. The CMCC-CM2-VHR4 models from hist-1950 and highresSST-present (Fig. 9m) were the only ones unable to capture both of these core clusters, although their magnitude was closer to CMIP and AMIP models. Overall, the HighResMIP models better represented the magnitude of both EWD's genesis and density, with the ECMWF models standing out (Fig. 9g, i, p, r).

Fig. 9 Tracking statistics at 850 hPa to the rainy season (AMJJA) of 1989-2009. Genesis density (left column) per unit area ($\sim 10^6$ km²) per season and Track density (right column) per unit area ($\sim 10^6$ km²) per season, of EWDs based on ERA5 (a, j) and CMIP models: NorESM2 (b, i), TaiESM1 (c, j); AMIP model: CMCC-CM2 (d, k), TaiESM1 (e, l); hist-1950 models: CMCC-CM2-VHR4 (f, m) and ECMWF-IFS-HR (g, n); highresSST models: CMCC-CM2-VHR4 (f, m) and ECMWF-IFS-HR (g, n). The continuous line corresponds to the values.

4 Conclusion

A comprehensive evaluation was conducted using 17 CMIP (historical), 16 AMIP, 7 hist-1950, and 10 highresSST-present models, focusing on their ability in replicating the annual and seasonal evolution of precipitation associated with EWDs over the southern tropical Atlantic. While the model ensembles exhibited consistent representations of precipitation, they struggled to accurately capture the precipitation intensity over the NEB coast, often underestimating it, while exhibiting overestimation in the northern NEB and TSA regions. A larger discrepancy between models and observations was found from January to June, with prevalent overestimation across most subareas. The highest uncertainty among the models was observed at the northern latitudes, whereas it was lower at the southern latitudes.

Analysis of normalized standard deviation and correlation revealed that better model performance was generally observed in regions south of the ITCZ, including the semi-arid and NEB coast, compared to those north of the ITCZ and adjacent TSA. On the other hand, standard deviations were better captured north of the ITCZ, indicating that despite higher correlation over some areas, certain models exhibited greater dispersion in the same areas.

CMIP models showed the poorest correlation and standard deviation, while highresSST-present models performed the best, a trend echoed across multiple statistical measures such as the RMSE and TSS. Top-performing models from each ensemble were identified, with atmospheric models, particularly those with higher resolutions, demonstrating superior performance compared to coupled models. Better performing models include CAS.FGOALS-f3-L and AS-RCEC.TaiESM1 in the CMIP and AMIP, with the AMIP version showcasing better results than its CMIP counterpart. CMCC.CMCC-CM2-SR5 emerged as the best-performing model among the AMIP models; however, in CMIP, it presented the lowest TSS values. In the hist-1950 and highresSST ensembles, CMCC-CM2-VHR4 and ECMWF.ECMWF-IFS-HR models emerged as top performers, particularly in their atmospheric versions. Overall, in our analysis, atmospheric models outperformed coupled models, especially those with higher resolutions (highresSST-present).

The three best-performing models in each set were selected: CMIP (AS-RCEC.TaiESM1, CAS.FGOALS-f3-L, and NCC.NorESM2-MM), AMIP (CAS.FGOALS-f3-L, AS-RCEC.TaiESM1, and CMCC.CMCC-CM2-SR5), hist-1950 (HadGEM3-GC31-HH, CMCC-CM2-VHR4, and ECMWF.ECMWF-IFS-HR), and highresSST (MRI.MRI-AGCM3-2-H, CMCC-CM2-VHR4, and ECMWF.ECMWF-IFS-HR).

Despite data limitations, the TRACK analysis was performed on a subset of models (9 out of 12), revealing mean lifetime (~6 days) and phase speed (~7 m s^{-1}) values of EWDs closely resembling ERA5 (5.78 days and 7.29 m s^{-1}), albeit with discrepancies in frequency. While ERA5 and climatological EWD frequencies showed opposite phases between 1989 and 1993, consistent variability patterns were still observed over time. However, most models overestimated EWD frequency (~45 EWDs $year^{-1}$) compared to ERA5 (~26 EWDs $year^{-1}$), except for a few models (e.g., NorESM2-MM, ~31 EWDs $year^{-1}$). The majority of models failed to reproduce the interannual variation in EWDs, except CMCC-CM2-SR5 (AMIP), NCC.NorESM2-MM (CMIP) and CMCC-CM2-VHR4 (hist-1950).

Two major genesis areas of EWDs were found from observations: one over the TSA and the other near the African coast. Models generally captured the key features observed in ERA5, aligning with known EWD formation systems. Most models successfully reproduced core positions near the NEB coast and the African west coast, with HighResMIP models, particularly those from ECMWF, demonstrating superior performance in capturing both core positions and magnitudes.

In conclusion, while improvements are still necessary, CMIP6 models exhibited promising capabilities in simulating spatial and temporal patterns in precipitation, as well as EWD characteristics over the NEB and adjacent TSA regions. Atmospheric models, especially those with higher spatial resolution, performed better, emphasizing the importance of higher resolution in model outcomes.

Acknowledments This study was supported by Conselho Nacional de Desenvolvimento Científico e Tecnológico, CNPq.

Data availability: Data available in a publicly accessible repository that does not issue DOIs Publicly available datasets were analyzed in this study. This data can be found here: [https://esgf-data.dkrz.de/search/cmip6-dkrz/], [https://measures.gesdisc.eosdis.nasa.gov/data/GPCP/GPCPMON.3.1/] and [https://cds.climate.copernicus.eu/cdsapp#!/dataset/reanalysis-era5-pressure-levels?tab=overview#!%2Fdataset%2Freanalysis-era5-single-levels%3Ftab=overview]

Conflicts of Interest: The authors declare no conflicts of interest.

References

Alves JMB (2001) Um vórtice ciclônico de altos níveis sobre o NEB e Atlântico adjacente no verão de 1999-2000. Revista Brasileira de Meteorologia 16(1): 115-122.

Asnani GC (1993) Tropical meteorology. Asnani, Indian Institute of Tropical Meteorology.

Babaousmail H, Hou R, Ayugi B, Ojara M, Ngoma H, Karim R, Rajasekar A, Ongoma V (2021) Evaluation of the performance of CMIP6 models in reproducing rainfall patterns over North Africa. Atmosphere 12(4):475.

Bazzanela AC, Dereczynski C, Luiz-Silva W, Regoto P (2023) Performance of CMIP6 models over South America. Climate Dynamics, pp. 1-16.

Chou SC (1990) Analysis of easterly wave disturbances over the South Equatorial Atlantic Ocean. Master Dissertation, National Institute for Space Research (in Portuguese).

Coutinho EC, Fisch G (2007) Easterly wave disturbances (EWDs) at the region of Alcântara Launching Center—MA. Braz J Meteorol 22(2):193–203 (in Portuguese)

Dias CG, Reboita MS (2021) Assessment of CMIP6 Simulations over Tropical South America. Revista Brasileira de Geografia Física 14:1282-1295.

Diedhiou A, Janicot S, Viltard A, Felice P (1998) Evidence of two regimes of easterly waves over West Africa and the tropical Atlantic. Geophysical Research Letters 25(15):2805-2808.

Dong T, Dong W (2021) Evaluation of extreme precipitation over Asia in CMIP6 models. Climate Dynamics, pp. 1-19.

Espinoza ES (1996) Disturbances in Easterly Winds in the Tropical Atlantic. Master Dissertation, National Institute for Space Research (in Portuguese).

Eyring V., Bony S, Meehl GA, Senior C, Stevens B, Stouffer RJ, Taylor KE (2015) Overview of the Coupled Model Intercomparison Project Phase 6 (CMIP6) experimental design and organization. Geoscientific Model Development Discussions 8(12).

Fan X, Duan Q, Shen C, Wu Y, Xing C (2020) Global surface air temperatures in CMIP6: historical performance and future changes. Environmental Research Letters 15(10):104056.

Fedorova N, Dos Santos DMB, Segundo MML, Levit V (2016) Middle Tropospheric Cyclonic Vortex in Northeastern Brazil and the Tropical Atlantic. Pure and Applied Geophysics 173:1-15.

Ferreira J, Chan CS, Satyamurti P (1990) Análise dos distúrbios ondulatórios de leste sobre o Oceano Atlântico Equatorial Sul. In: ANAIS do VI CONGRESSO BRASILEIRO DE METEOROLOGIA, Salvador, pp. 462-468.

Firpo MAF, Guimarães BDS, Dantas LG, Silva MGBD, Alves LM, Chadwick R, Llopart MA, Oliveira GSD (2022) Assessment of CMIP6 models' performance in simulating present day climate in Brazil. Frontiers in Climate, pp. 170.

Gomes HB, Ambrizzi T, Herdies DL, Hodges K, Pontes da Silva BF (2015) Easterly wave disturbances over Northeast Brazil: an observational analysis. Advances in Meteorology 2015:1-20.

Gomes HB, Ambrizzi T, Pontes da Silva BF, Hodges K, Silva Dias PL, Herdies DL, Silva MCL, Gomes HB (2019) Climatology of easterly wave disturbances over the tropical South Atlantic. Climate Dynamics 53(3):1393-1411.

Gan MA, Kousky VE (1986) Vórtices ciclônicos da alta troposfera no oceano Atlântico Sul. Revista Brasileira de Meteorologia 1(1):19-28.

Haarsma RJ, Roberts MJ, Vidale PL, Senior CA, Bellucci A, Bao Q (2016) High resolution model intercomparison project (HighResMIP v1. 0) for CMIP6. Geoscientific Model Development 9(11):4185-4208.

Hastenrath S, Heller L (1977) Dynamics of climatic hazards in Northeast Brazil. Quarterly Journal of the Royal Meteorological Society 103:77-92.

Hollis MA, Mccrary RR, Stachnik JP, Lewis-Merritt C, Martin ER (2023) A global climatology of tropical easterly waves. Climate Dynamics, pp. 1-16.

Hodges KI (1995) Feature Tracking on the Unit Sphere. Monthly Weather Review 123: 3458-3465.

Hodges KI (1999) Adaptive constraints for feature tracking. Monthly Weather Review 127(6), 1362-1373.

Hopsch SB, Thorncroft CD, Hodges KI, Aiyyer A (2007) West African storm tracks and their relationship to Atlantic tropical cyclones. Journal of Climate 20(11):2468-2483.

Huffman GJ, Behrangi A, Bolvin DT, Nelkin E (2020) GPCP Version 3.1 Satellite-Gauge (SG) Combined Precipitation Data Set. NASA GES DISC: Greenbelt, MD, USA.

Kayano MT (1979) A climatic and synoptic study using radiosonde data (1968–1976) from Manaus and Belem. Master Dissertation, National Institute for Space Research (in Portuguese)

Kousky VE (1979) Frontal Influences on Northeast Brazil. Monthly Weather Review 107: 1140-1153.

Kousky VE (1980) Diurnal rainfall variation in northeast Brazil. Monthly Weather Review 108(4):488-498.

Kousky VE, Gan MA (1981) Upper tropospheric cyclonic vortices in the tropical South Atlantic. Tellus 33(6):538-551.

Lyra MJA, Gomes HB, Herdies DL, Ramirez E, Cavalcante LCV, de Freitas IGF, Aravéquia JA, Figueroa SN, da Silva, MCL, Silva FDS, Gomes HB; Vendrasco EP, Calvetti L, Mantovani, JA, Pendharkar J, Coelho W, de Quadro, MFL, Roberti, DR, Beneti CAA (2024). Extreme precipitation events over the east coast of northeast Brazil: Synoptic study and MPAS simulation. Weather and Climate Extremes 45:100711.

Medeiros FJ, De Oliveira CP, Avila-Diaz (2022) A Evaluation of extreme precipitation climate indices and their projected changes for Brazil: From CMIP3 to CMIP6. Weather and Climate Extremes 38:100511.

Melo ABC, Cavalcanti IFA, Souza PP (2009) Zona de convergência intertropical do atlântico. In: Cavalcanti IFA, Ferreira NJ, Silva MGAJ, Dias MAFS Tempo e clima no Brasil. Oficina de textos. São Paulo.

Metrópoles (2022) Chuvas causam pelo menos 35 mortes e destruição no Recife e região. https://www.metropoles.com/brasil/chuvas-causam-pelo-menos-33-mortes-e-destruicao-no-recife-e-regiao (accessed 21 February 2024).

Metrópoles (2022) Tragédia em Pernambuco: governador pede apoio das Forças Armadas. https://www.metropoles.com/brasil/tragedia-em-pernambuco-governador-pede-apoio-das-forcas-armadas (accessed 21 February 2024).

Molion LCB, Bernardo SO (2002) Uma Revisão da Dinâmica das Chuvas no Nordeste Brasileiro. Revista Brasileira de Meteorologia 17(1):1-10.

Motas GV (1997) Observational study of easterly wave disturbances over the northeastern Brazil. Master Dissertation, University of São Paulo (in Portuguese)

Neiva EJF (1975) An investigations of wave-type disturbances over the tropical South Atlantic Ocean. M.Sc. Thesis, Naval Post Gradu- ate School.

Ngoma H, Wen W, Ayugi B, Babaousmail H, Karim R, Ongoma V (2021) Evaluation of precipitation simulations in CMIP6 models over Uganda. International Journal of Climatology 41(9):4743-4768.

Nobre P (1994) On the genesis of anomalous SST and rainfall patterns over the tropical Atlantic, pp. 3128-3128.

Nobre P, Shukla J (1996) Variations of sea surface temperature, wind stress and rainfall over the tropical Atlantic and South America. Journal of climate 9:2464-2479.

Oliveira PD, Santos E Silva CM, Lima KC (2017) Climatology and trend analysis of extreme precipitation in subregions of Northeast Brazil. Theoretical and Applied Climatology 130:77-90.

Ortega G, Arias PA, Villegas JC, Marquet PA, Nobre P (2021) Present-day and future climate over central and South America according to CMIP5/CMIP6 models. International Journal of Climatology 41(15):6713-6735.

Pontes da Silva BF (2011) Easterly Waves contribution for the east- ern northeast Brazil precipitation: mean synoptic evolution and numerical simulations. Master Dissertation, University of São Paulo (in Portuguese)

Rao VB, Lima MC, Franchito SH (1993) Seasonal and interannual variations of rainfall over eastern northeast Brazil. Journal of climate 6(9):1754-1763.

Reboita MS, Gan MA, Rocha RPD, Ambrizzi T (2010) Regimes de precipitação na América do Sul: uma revisão bibliográfica. Revista Brasileira de Meteorologia 25(2):185-204.

Rivera JA, Arnould G (2020) Evaluation of the ability of CMIP6 models to simulate precipitation over Southwestern South America: Climatic features and long-term trends (1901–2014). Atmospheric Research 241:104953.

Rodrigues DT, Gonçalves WA, Spyrides MHC, Santos e Silva CM (2020) Spatial and temporal assessment of the extreme and daily precipitation of the Tropical Rainfall Measuring Mission satellite in Northeast Brazil. International Journal of Remote Sensing 41(2):549-572.

Serra YL, Kiladis GN, Hodges KI (2010) Tracking and mean structure of easterly waves over the intra-Americas sea. Journal of Climate 23:4823–4840.

Shiru MS, Chung ES (2021) Performance evaluation of CMIP6 global climate models for selecting models for climate projection over Nigeria. Theoretical and Applied Climatology, pp. 1-17.

Taylor KE (2001) Summarizing multiple aspects of model performance in a single diagram. Journal of Geophysical Research: Atmospheres 106:7183-7192.

Torres RR, Ferreira NJ (2011) Case studies of easterly wave disturbances over Northeast Brazil using the Eta Model. Weather and Forecasting 26(2):225-235.

Thorncroft CD, Hodges KI (2001) African Easterly Wave Variability and its Relationship to Atlantic Tropical Cyclone Activity. Journal of Climate 14:1166- 1179.

Touzé-peiffer L, Barberousse A, Le Treut H (2020) The Coupled Model Intercomparison Project: History, uses, and structural effects on climate research. Wiley Interdisciplinary Reviews: Climate Change 11(4):648.

Tukey JW (1977) Exploratory data analysis. v. 2:131-160.

Xie P, Arkin PA (1997) Global precipitation: A 17-year monthly analysis based on gauge observations, satellite estimates, and numerical model outputs. Bulletin of the american meteorological society 78(11):2539-2558.

Yamazaki Y (1995) Theoretical and synoptic studies of tropical disturbances. Master Dissertation, National Institute for Space Research (in Portuguese).

Yamazaki Y, Rao VB (1977) Tropical cloudiness over the south Atlantic Ocean. Journal of the Meteorological Society of Japan. Ser. II 55(2):205-207.

Fig. 4

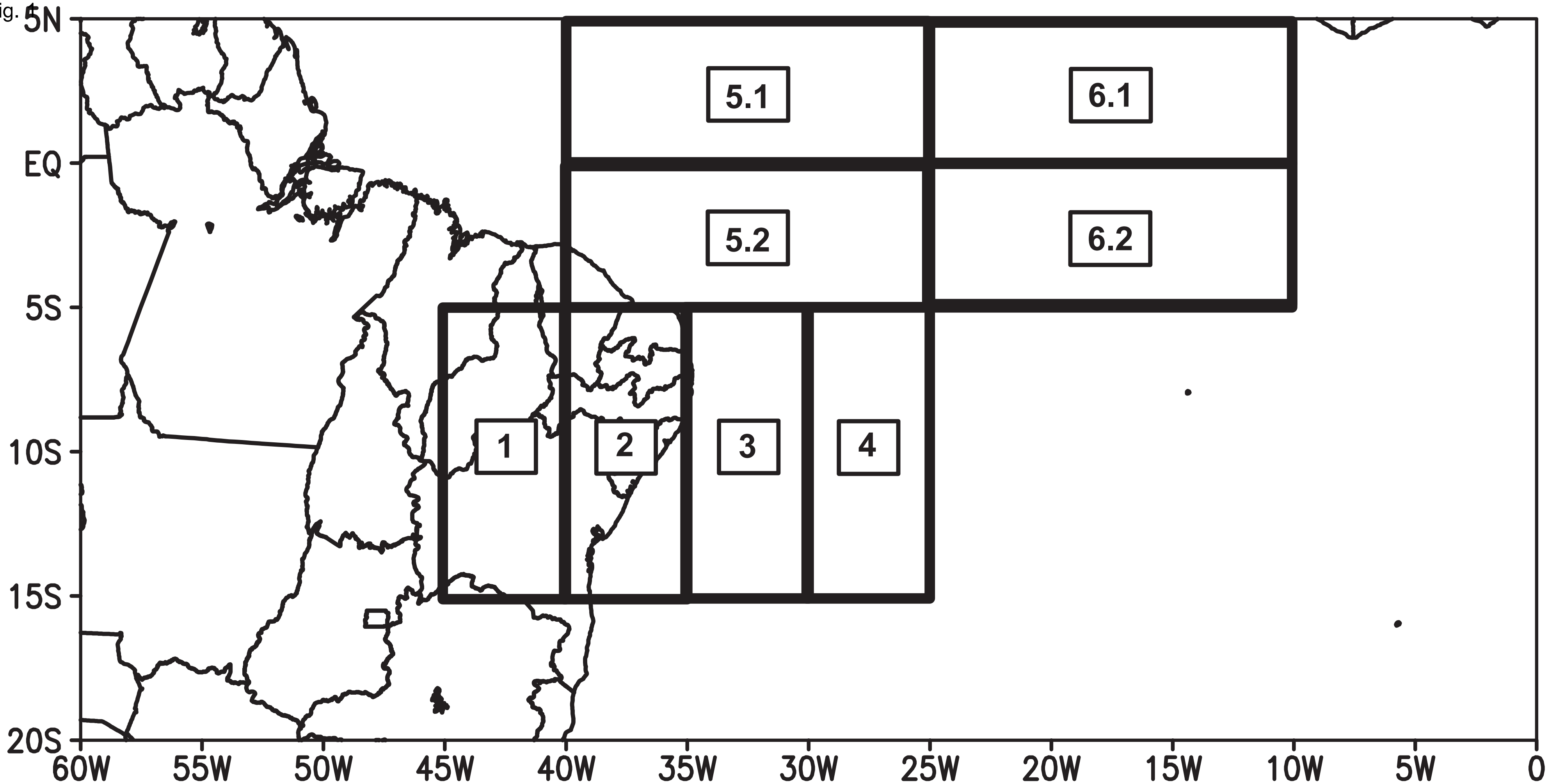

5.1
6.1
5.2
6.2
1
2
3
4
5N
EQ
5S
10S
15S
20S
60W
55W
50W
45W
40W
35W
30W
25W
20W
15W
10W
5W
0

Fig. 2

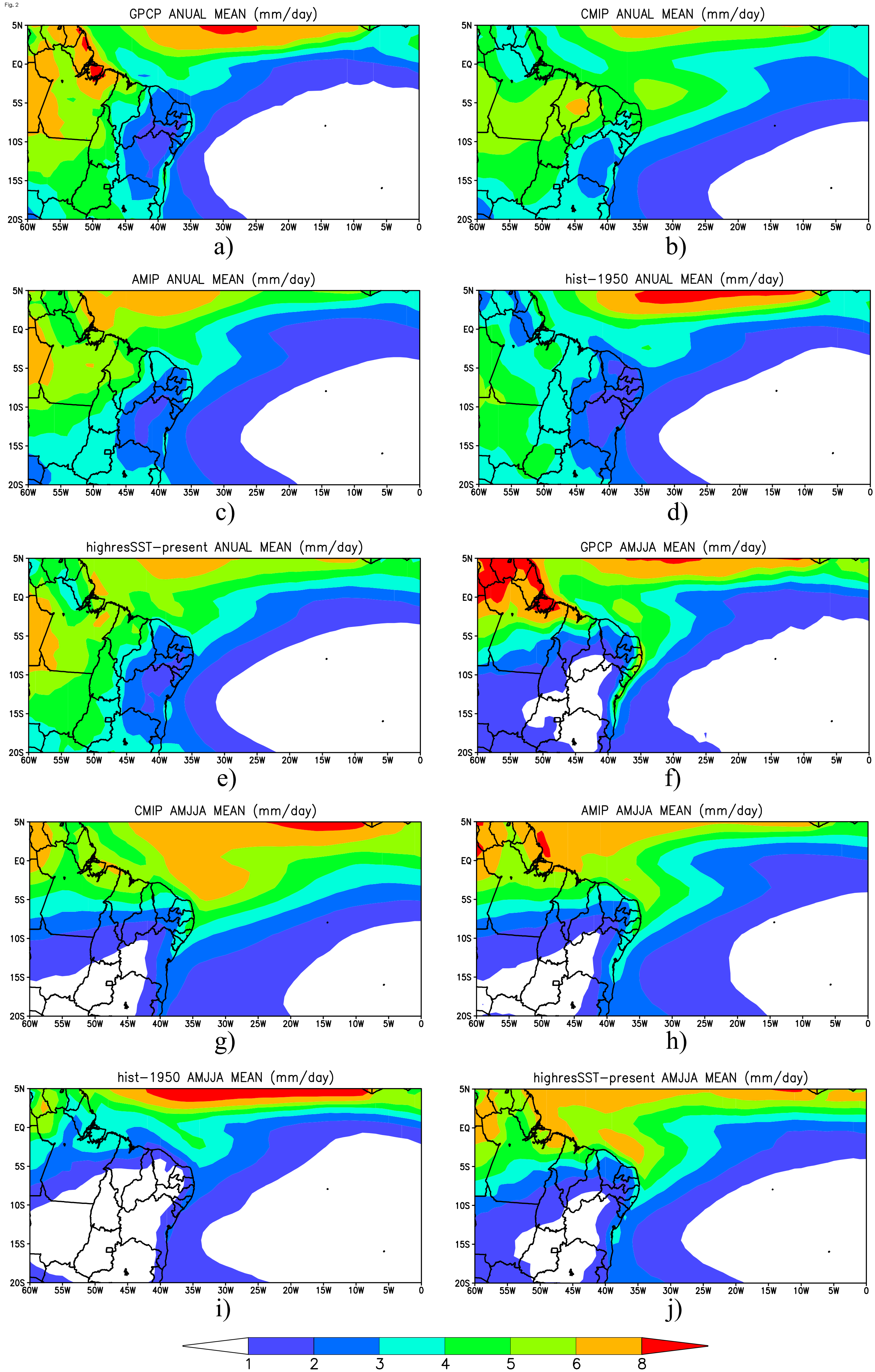

GPCP ANUAL MEAN (mm/day)
a)
CMIP ANUAL MEAN (mm/day)
b)
AMIP ANUAL MEAN (mm/day)
c)
hist-1950 ANUAL MEAN (mm/day)
d)
highresSST-present ANUAL MEAN (mm/day)
e)
GPCP AMJJA MEAN (mm/day)
f)
CMIP AMJJA MEAN (mm/day)
g)
AMIP AMJJA MEAN (mm/day)
h)
hist-1950 AMJJA MEAN (mm/day)
i)
highresSST-present AMJJA MEAN (mm/day)
j)
5N EQ 5S 10S 15S 20S
60W 55W 50W 45W 40W 35W 30W 25W 20W 15W 10W 5W 0
1 2 3 4 5 6 8

Fig. 3

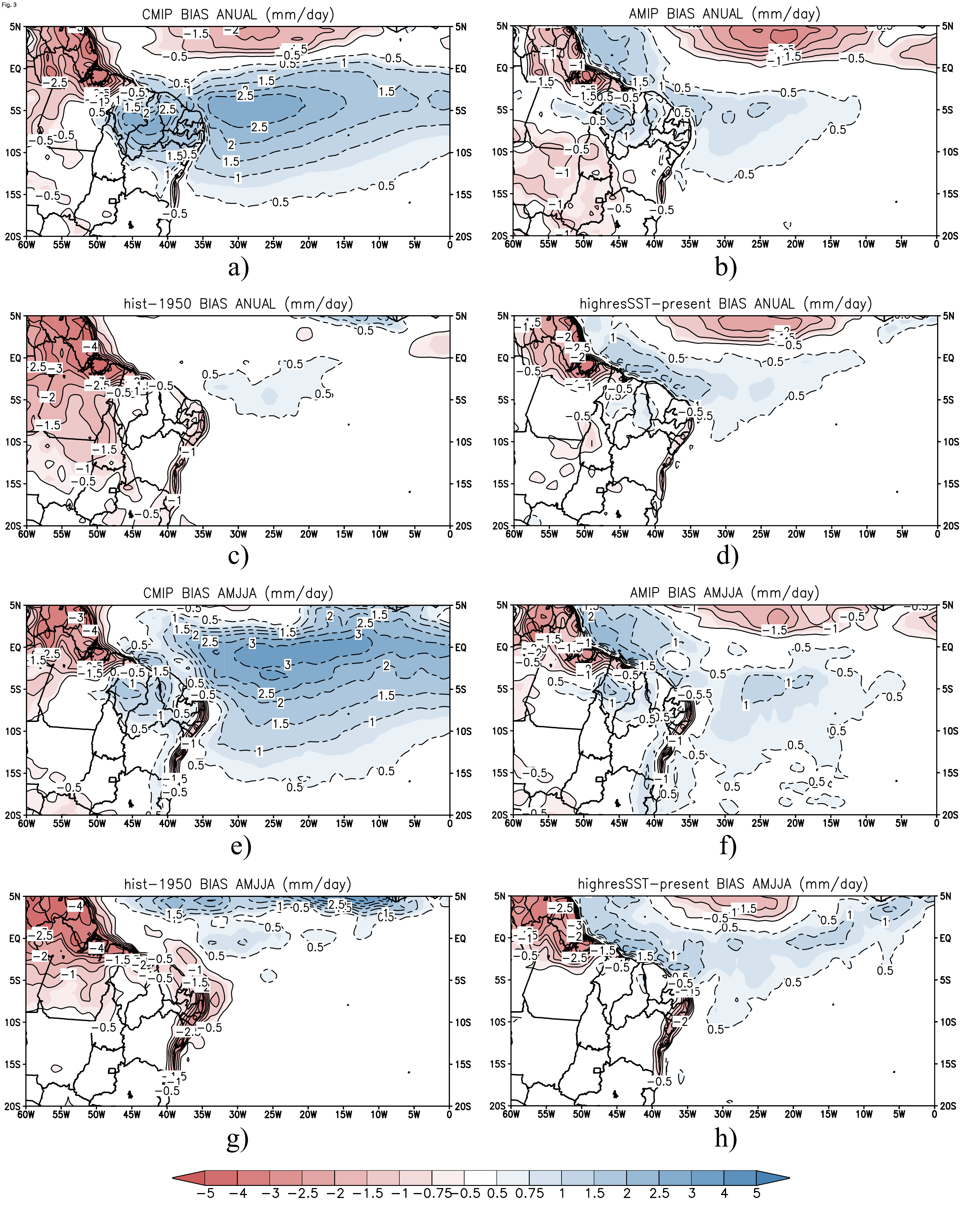
CMIP BIAS ANUAL (mm/day)
a)
AMIP BIAS ANUAL (mm/day)
b)
hist-1950 BIAS ANUAL (mm/day)
c)
highresSST-present BIAS ANUAL (mm/day)
d)
CMIP BIAS AMJJA (mm/day)
e)
AMIP BIAS AMJJA (mm/day)
f)
hist-1950 BIAS AMJJA (mm/day)
g)
highresSST-present BIAS AMJJA (mm/day)
h)
−5 −4 −3 −2.5 −2 −1.5 −1 −0.75 −0.5 0.5 0.75 1 1.5 2 2.5 3 4 5

Fig. 4

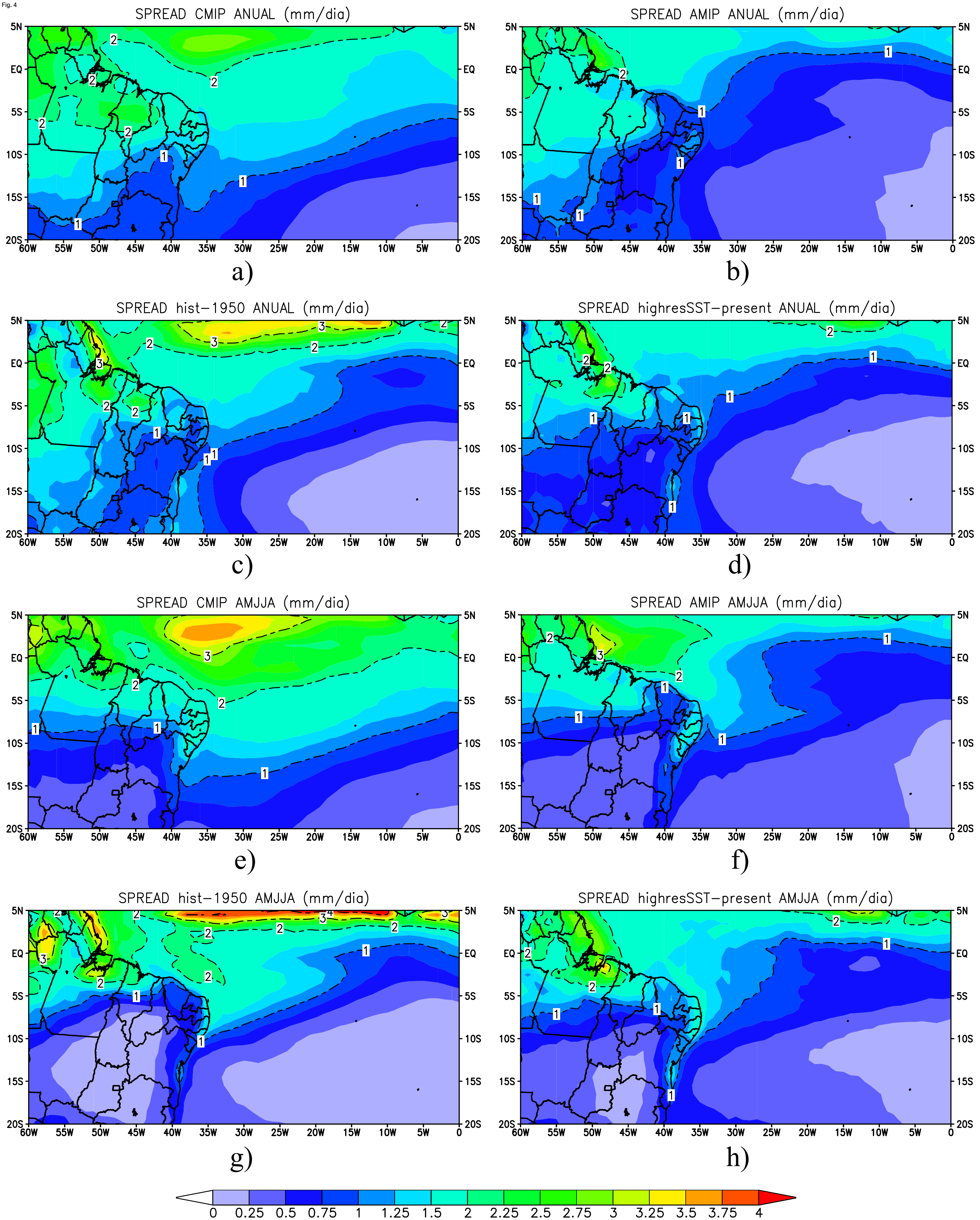

SPREAD CMIP ANUAL (mm/dia)
a)
SPREAD AMIP ANUAL (mm/dia)
b)
SPREAD hist−1950 ANUAL (mm/dia)
c)
SPREAD highresSST−present ANUAL (mm/dia)
d)
SPREAD CMIP AMJJA (mm/dia)
e)
SPREAD AMIP AMJJA (mm/dia)
f)
SPREAD hist−1950 AMJJA (mm/dia)
g)
SPREAD highresSST−present AMJJA (mm/dia)
h)
0 0.25 0.5 0.75 1 1.25 1.5 2 2.25 2.5 2.75 3 3.25 3.5 3.75 4

Fig. 5

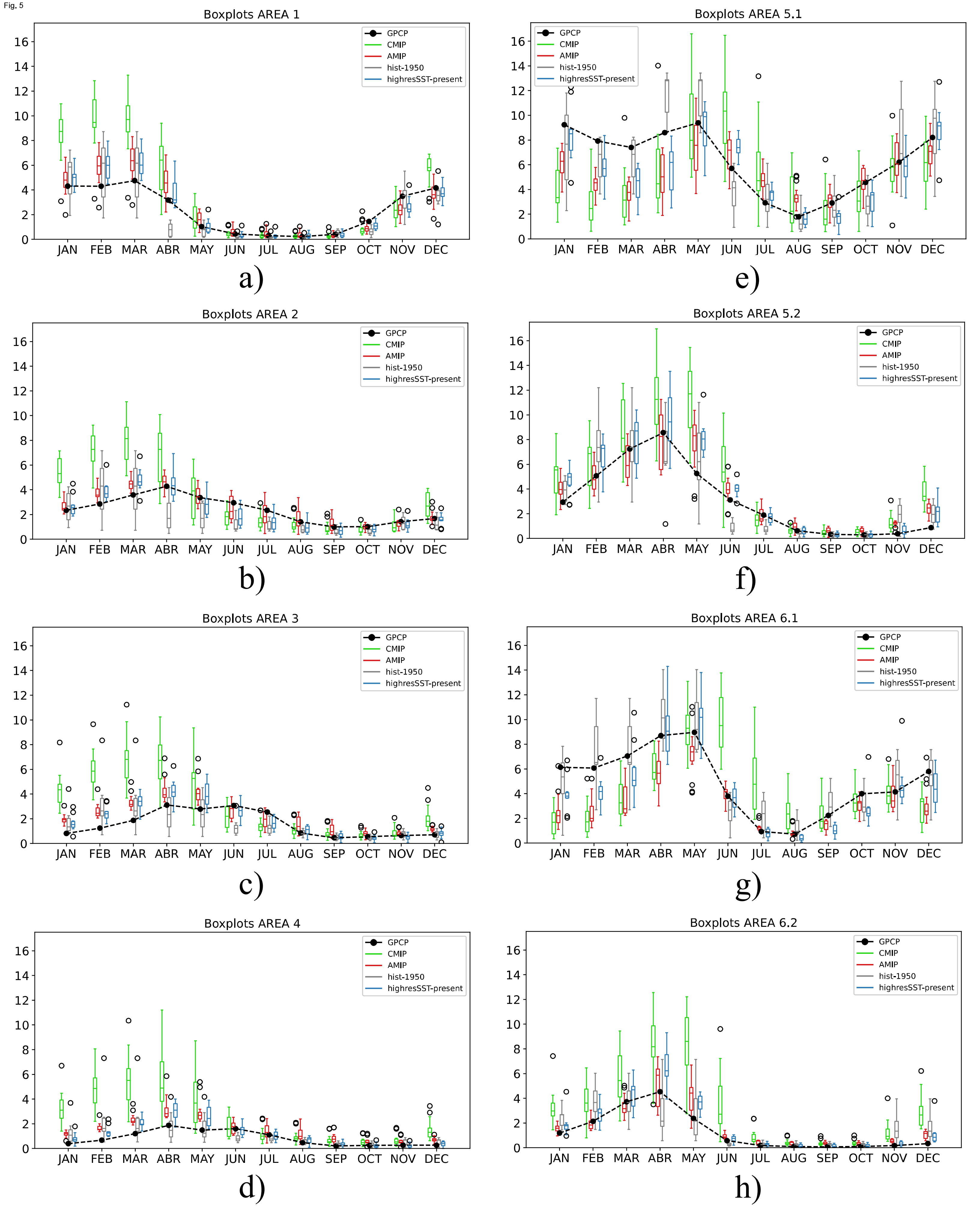

Boxplots AREA 1
a)
Boxplots AREA 2
b)
Boxplots AREA 3
c)
Boxplots AREA 4
d)
Boxplots AREA 5.1
e)
Boxplots AREA 5.2
f)
Boxplots AREA 6.1
g)
Boxplots AREA 6.2
h)
GPCP
CMIP
AMIP
hist-1950
highresSST-present
JAN FEB MAR ABR MAY JUN JUL AUG SEP OCT NOV DEC
0 2 4 6 8 10 12 14 16

Fig. 6

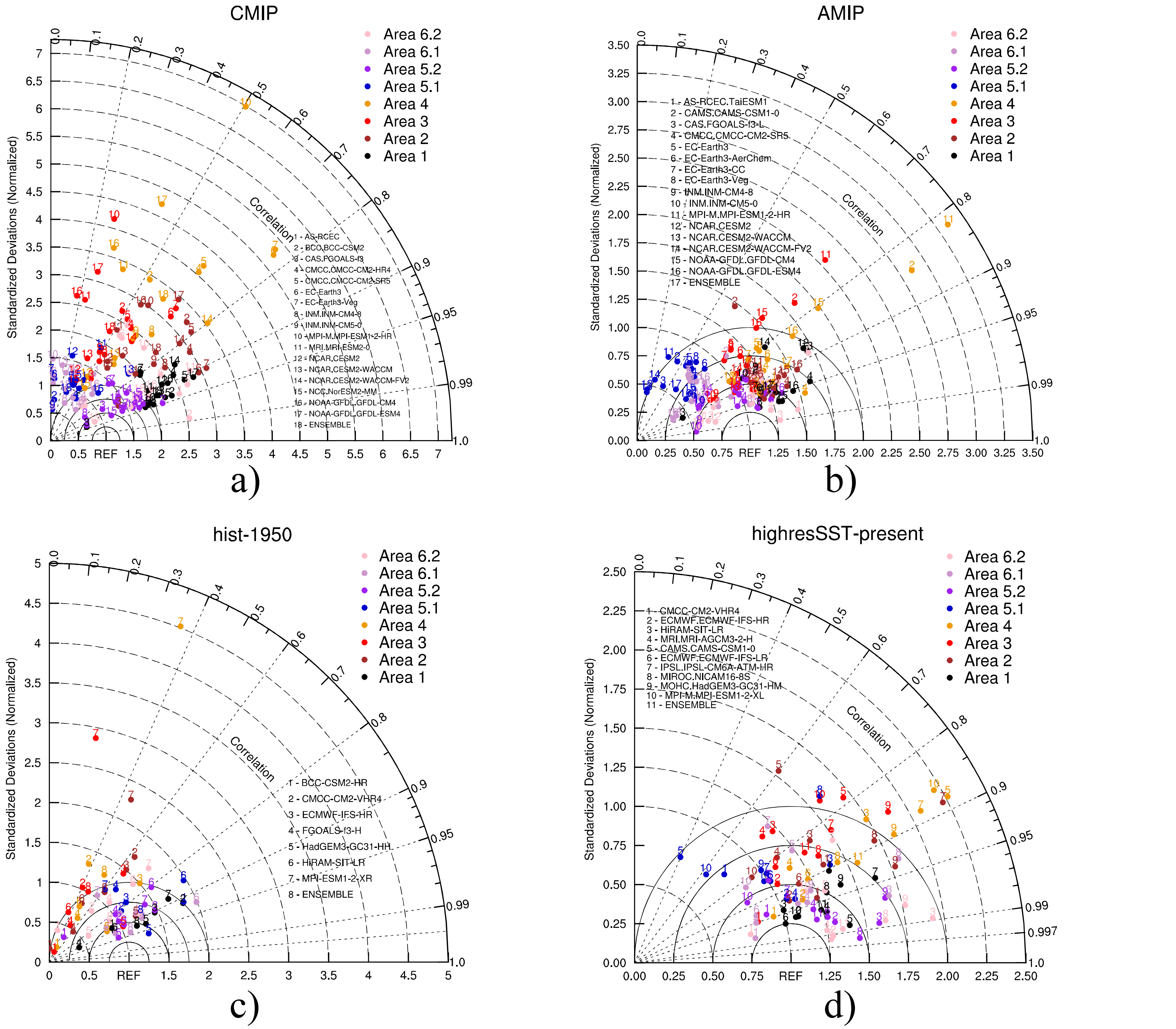
CMIP
AMIP
hist-1950
highresSST-present
Area 6.2
Area 6.1
Area 5.2
Area 5.1
Area 4
Area 3
Area 2
Area 1
Standardized Deviations (Normalized)
Correlation
REF
1 - AS-RCEC
2 - BCC.BCC-CSM2
3 - CAS.FGOALS-f3
4 - CMCC.CMCC-CM2-HR4
5 - CMCC.CMCC-CM2-SR5
6 - EC-Earth3
7 - EC-Earth3-Veg
8 - INM.INM-CM4-8
9 - INM.INM-CM5-0
10 - MPI-M.MPI-ESM1-2-HR
11 - MRI.MRI-ESM2-0
12 - NCAR.CESM2
13 - NCAR.CESM2-WACCM
14 - NCAR.CESM2-WACCM-FV2
15 - NCC.NorESM2-MM
16 - NOAA-GFDL.GFDL-CM4
17 - NOAA-GFDL.GFDL-ESM4
18 - ENSEMBLE
1 - AS-RCEC.TaiESM1
2 - CAMS.CAMS-CSM1-0
3 - CAS.FGOALS-f3-L
4 - CMCC.CMCC-CM2-SR5
5 - EC-Earth3
6 - EC-Earth3-AerChem
7 - EC-Earth3-CC
8 - EC-Earth3-Veg
9 - INM.INM-CM4-8
10 - INM.INM-CM5-0
11 - MPI-M.MPI-ESM1-2-HR
12 - NCAR.CESM2
13 - NCAR.CESM2-WACCM
14 - NCAR.CESM2-WACCM-FV2
15 - NOAA-GFDL.GFDL-CM4
16 - NOAA-GFDL.GFDL-ESM4
17 - ENSEMBLE
1 - BCC-CSM2-HR
2 - CMCC-CM2-VHR4
3 - ECMWF-IFS-HR
4 - FGOALS-f3-H
5 - HadGEM3-GC31-HH
6 - HiRAM-SIT-LR
7 - MPI-ESM1-2-XR
8 - ENSEMBLE
1 - CMCC-CM2-VHR4
2 - ECMWF.ECMWF-IFS-HR
3 - HiRAM-SIT-LR
4 - MRI.MRI-AGCM3-2-H
5 - CAMS.CAMS-CSM1-0
6 - ECMWF.ECMWF-IFS-LR
7 - IPSL.IPSL-CM6A-ATM-HR
8 - MIROC.NICAM16-8S
9 - MOHC.HadGEM3-GC31-HM
10 - MPI-M.MPI-ESM1-2-XL
11 - ENSEMBLE
a)
b)
c)
d)

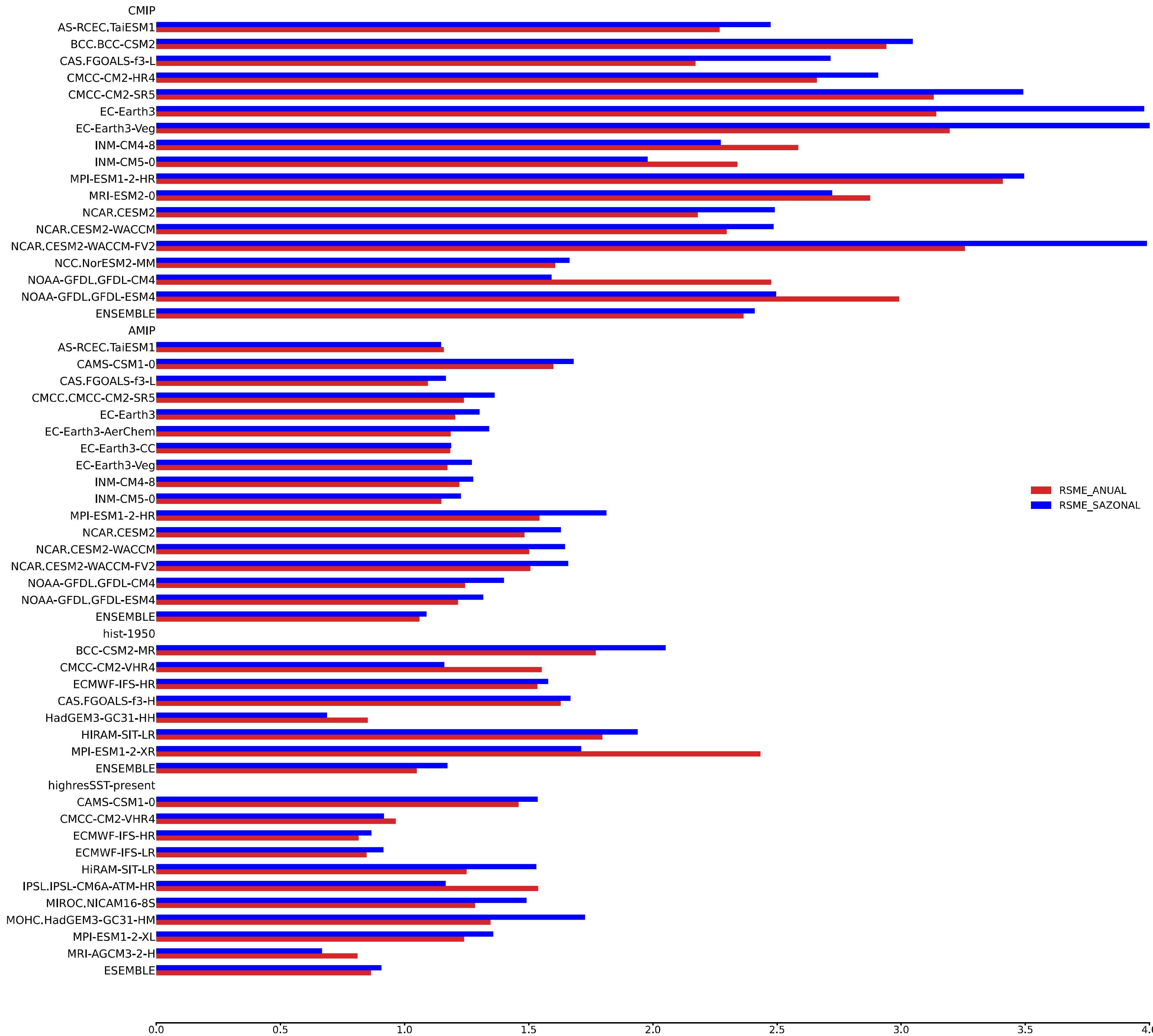
CMIP
AS-RCEC.TaiESM1
BCC.BCC-CSM2
CAS.FGOALS-f3-L
CMCC-CM2-HR4
CMCC-CM2-SR5
EC-Earth3
EC-Earth3-Veg
INM-CM4-8
INM-CM5-0
MPI-ESM1-2-HR
MRI-ESM2-0
NCAR.CESM2
NCAR.CESM2-WACCM
NCAR.CESM2-WACCM-FV2
NCC.NorESM2-MM
NOAA-GFDL.GFDL-CM4
NOAA-GFDL.GFDL-ESM4
ENSEMBLE
AMIP
AS-RCEC.TaiESM1
CAMS-CSM1-0
CAS.FGOALS-f3-L
CMCC.CMCC-CM2-SR5
EC-Earth3
EC-Earth3-AerChem
EC-Earth3-CC
EC-Earth3-Veg
INM-CM4-8
INM-CM5-0
MPI-ESM1-2-HR
NCAR.CESM2
NCAR.CESM2-WACCM
NCAR.CESM2-WACCM-FV2
NOAA-GFDL.GFDL-CM4
NOAA-GFDL.GFDL-ESM4
ENSEMBLE
hist-1950
BCC-CSM2-MR
CMCC-CM2-VHR4
ECMWF-IFS-HR
CAS.FGOALS-f3-H
HadGEM3-GC31-HH
HIRAM-SIT-LR
MPI-ESM1-2-XR
ENSEMBLE
highresSST-present
CAMS-CSM1-0
CMCC-CM2-VHR4
ECMWF-IFS-HR
ECMWF-IFS-LR
HiRAM-SIT-LR
IPSL.IPSL-CM6A-ATM-HR
MIROC.NICAM16-8S
MOHC.HadGEM3-GC31-HM
MPI-ESM1-2-XL
MRI-AGCM3-2-H
ESEMBLE
RSME_ANUAL
RSME_SAZONAL
0.0
0.5
1.0
1.5
2.0
2.5
3.0
3.5
4.0

a)

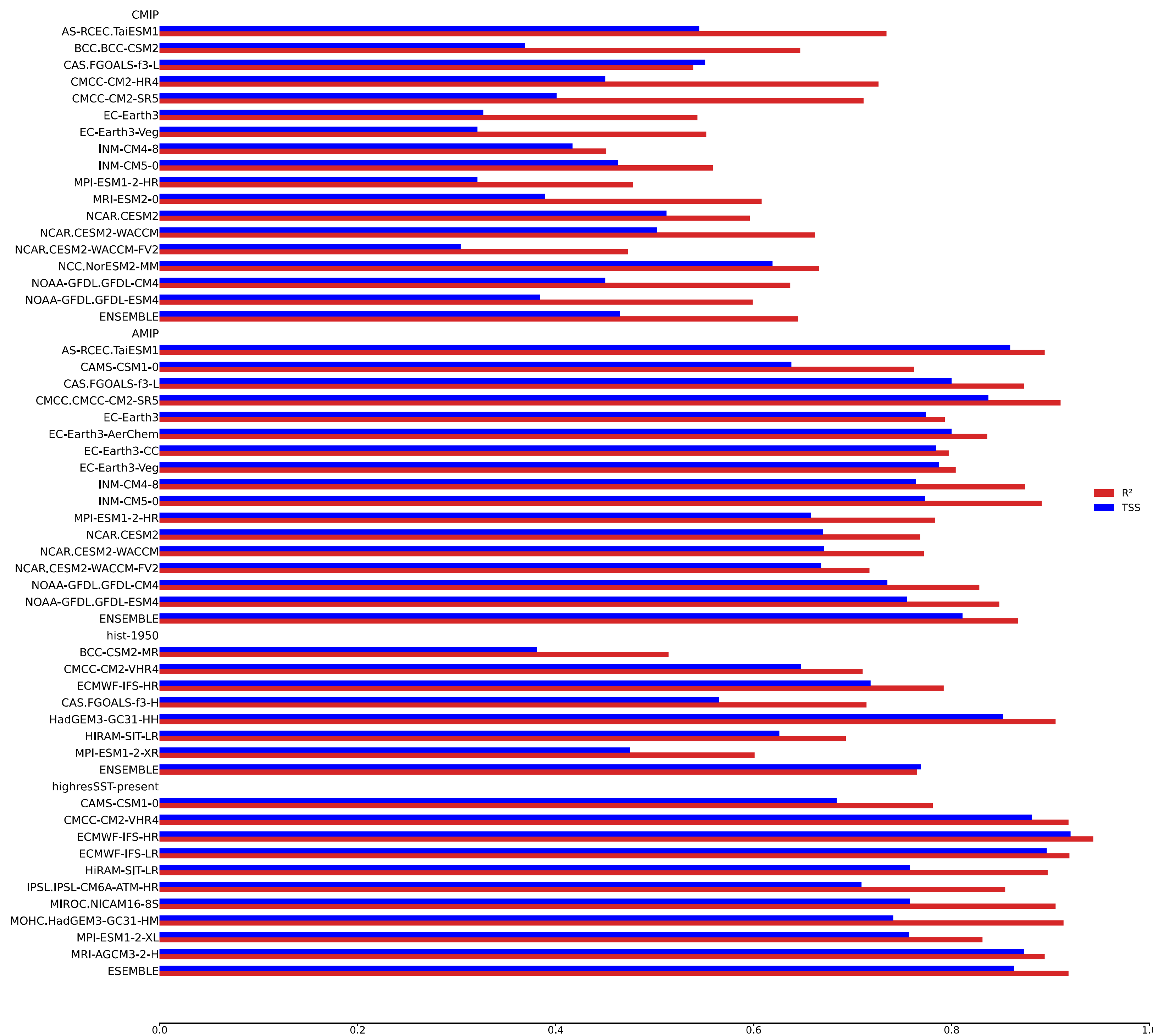

CMIP
AS-RCEC.TaiESM1
BCC.BCC-CSM2
CAS.FGOALS-f3-L
CMCC-CM2-HR4
CMCC-CM2-SR5
EC-Earth3
EC-Earth3-Veg
INM-CM4-8
INM-CM5-0
MPI-ESM1-2-HR
MRI-ESM2-0
NCAR.CESM2
NCAR.CESM2-WACCM
NCAR.CESM2-WACCM-FV2
NCC.NorESM2-MM
NOAA-GFDL.GFDL-CM4
NOAA-GFDL.GFDL-ESM4
ENSEMBLE
AMIP
AS-RCEC.TaiESM1
CAMS-CSM1-0
CAS.FGOALS-f3-L
CMCC.CMCC-CM2-SR5
EC-Earth3
EC-Earth3-AerChem
EC-Earth3-CC
EC-Earth3-Veg
INM-CM4-8
INM-CM5-0
MPI-ESM1-2-HR
NCAR.CESM2
NCAR.CESM2-WACCM
NCAR.CESM2-WACCM-FV2
NOAA-GFDL.GFDL-CM4
NOAA-GFDL.GFDL-ESM4
ENSEMBLE
hist-1950
BCC-CSM2-MR
CMCC-CM2-VHR4
ECMWF-IFS-HR
CAS.FGOALS-f3-H
HadGEM3-GC31-HH
HIRAM-SIT-LR
MPI-ESM1-2-XR
ENSEMBLE
highresSST-present
CAMS-CSM1-0
CMCC-CM2-VHR4
ECMWF-IFS-HR
ECMWF-IFS-LR
HiRAM-SIT-LR
IPSL.IPSL-CM6A-ATM-HR
MIROC.NICAM16-8S
MOHC.HadGEM3-GC31-HM
MPI-ESM1-2-XL
MRI-AGCM3-2-H
ESEMBLE
R²
TSS
0.0
0.2
0.4
0.6
0.8
1.0

b)

Fig. 8

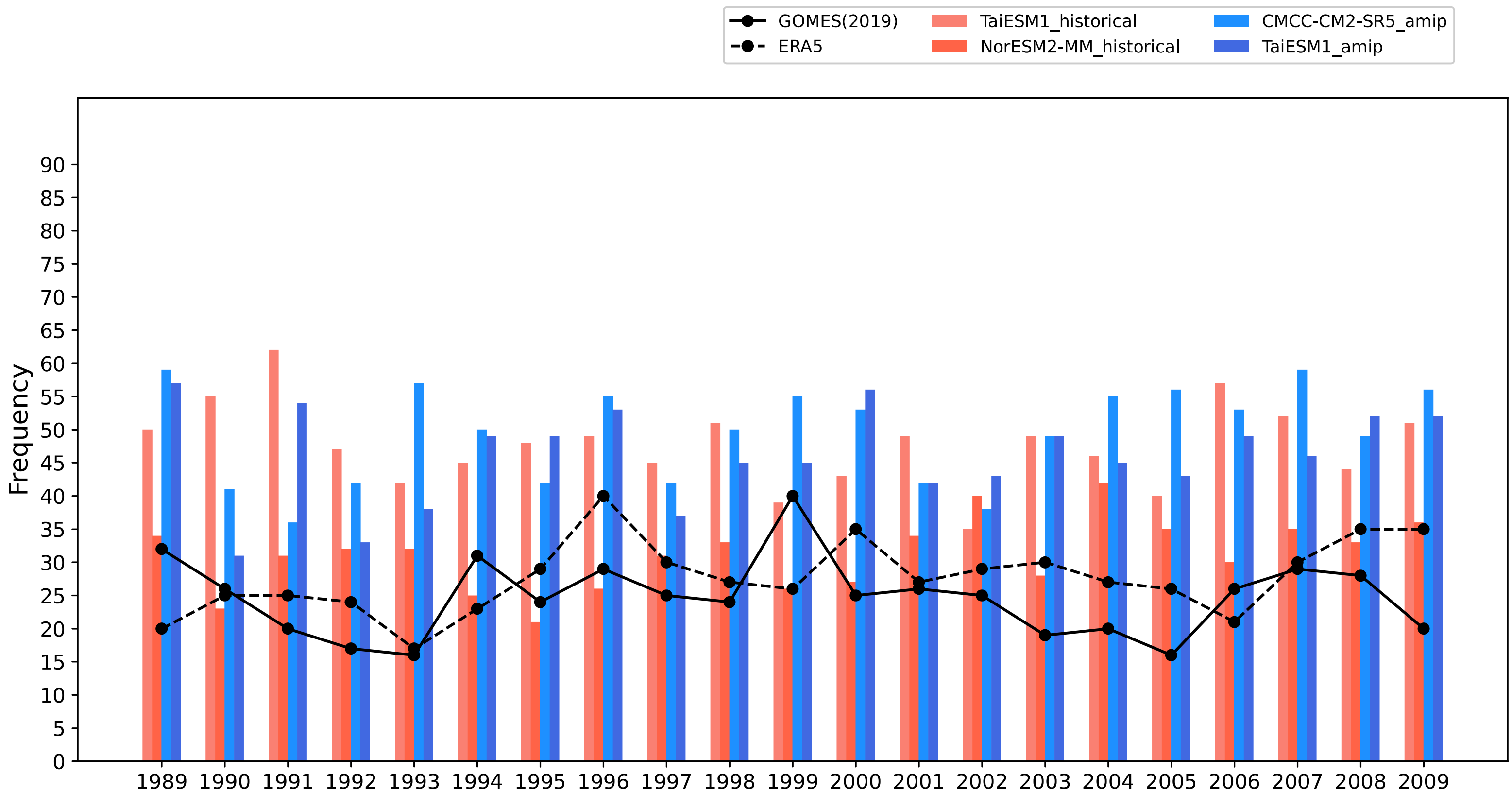
GOMES(2019)
ERA5
TaiESM1_historical
NorESM2-MM_historical
CMCC-CM2-SR5_amip
TaiESM1_amip
Frequency
1989 1990 1991 1992 1993 1994 1995 1996 1997 1998 1999 2000 2001 2002 2003 2004 2005 2006 2007 2008 2009

a)

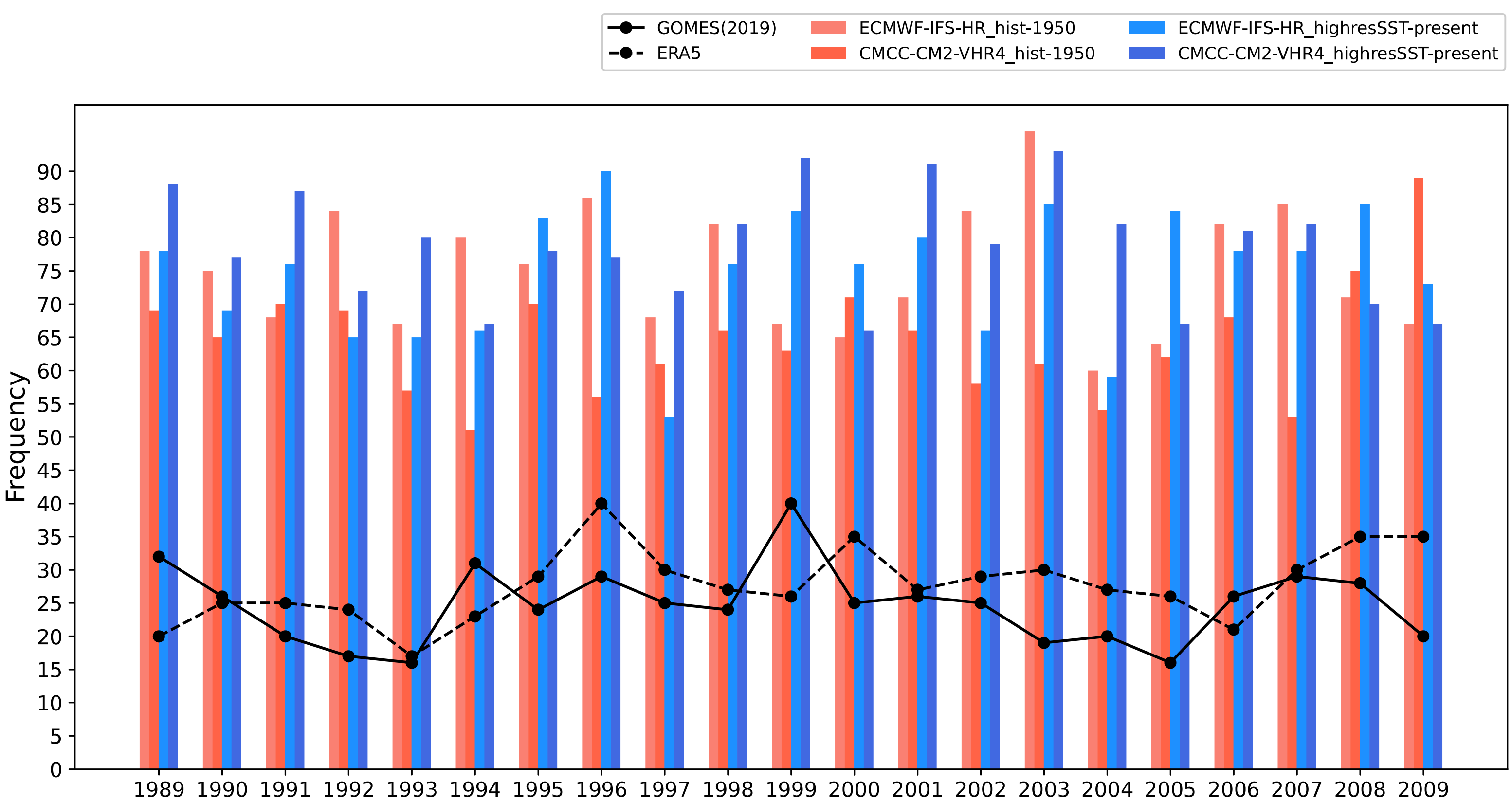
GOMES(2019)
ERA5
ECMWF-IFS-HR_hist-1950
CMCC-CM2-VHR4_hist-1950
ECMWF-IFS-HR_highresSST-present
CMCC-CM2-VHR4_highresSST-present
Frequency
1989 1990 1991 1992 1993 1994 1995 1996 1997 1998 1999 2000 2001 2002 2003 2004 2005 2006 2007 2008 2009

b)

Fig. 9

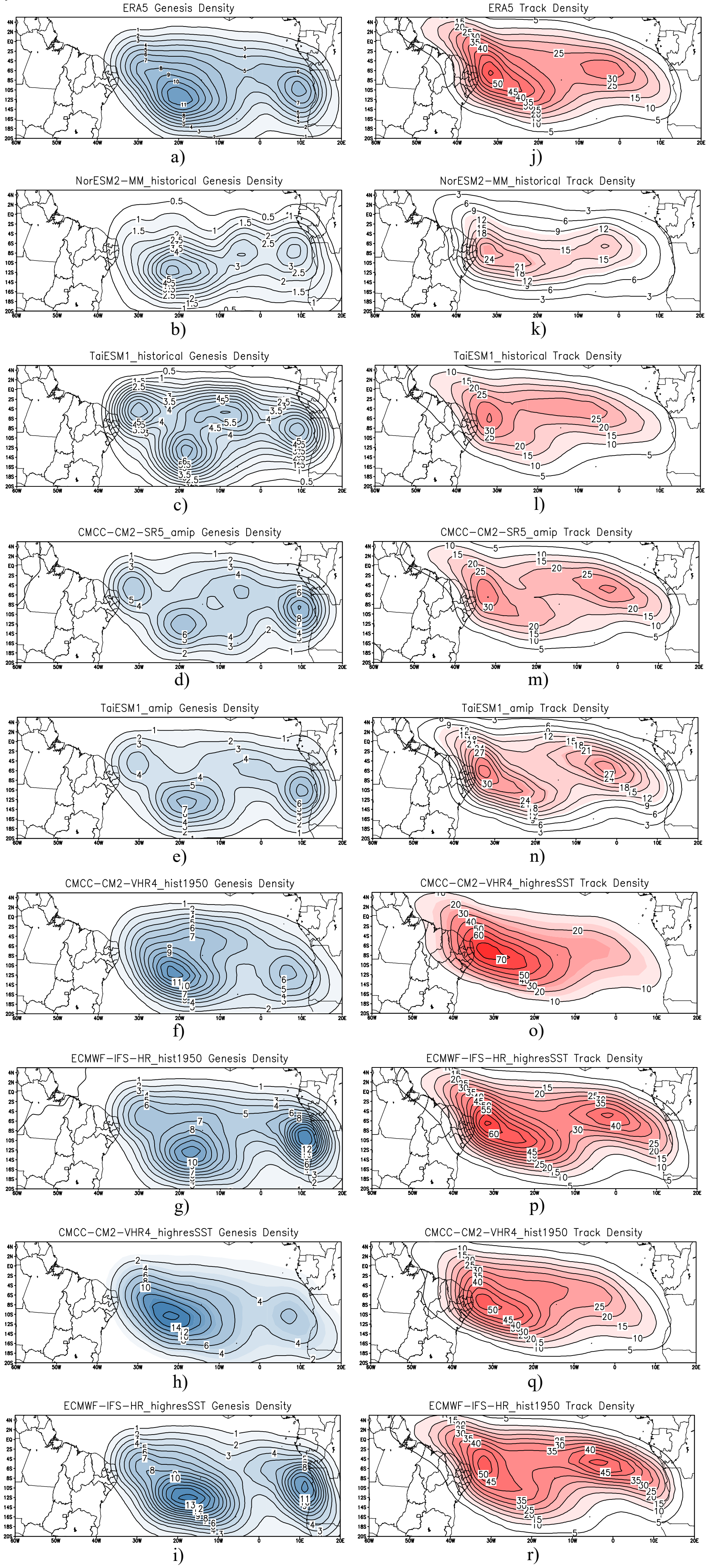
ERA5 Genesis Density
ERA5 Track Density
a)
j)
NorESM2-MM_historical Genesis Density
NorESM2-MM_historical Track Density
b)
k)
TaiESM1_historical Genesis Density
TaiESM1_historical Track Density
c)
l)
CMCC-CM2-SR5_amip Genesis Density
CMCC-CM2-SR5_amip Track Density
d)
m)
TaiESM1_amip Genesis Density
TaiESM1_amip Track Density
e)
n)
CMCC-CM2-VHR4_hist1950 Genesis Density
CMCC-CM2-VHR4_highresSST Track Density
f)
o)
ECMWF-IFS-HR_hist1950 Genesis Density
ECMWF-IFS-HR_highresSST Track Density
g)
p)
CMCC-CM2-VHR4_highresSST Genesis Density
CMCC-CM2-VHR4_hist1950 Track Density
h)
q)
ECMWF-IFS-HR_highresSST Genesis Density
ECMWF-IFS-HR_hist1950 Track Density
i)
r)

Table 1

Period (days)	Wavelength (km)	Phase velocity (ms^{-1})	Levels (hPa)	Methods/Data	References
4-6	6000	14	700-300	v, spectral analysis	Neiva 1975
4	4000	10	-	Satellite	Yamazaki 1975
3-5	-	12	-	Sounding	Kayano 1979
3-6	6200	12	850	v, ROLE, spectral analysis	Chou 1990
4	3500-4500	10-13	1000-500	v, EOF and EEOF	Espinoza 1996
3.5-3.8	2900-3800	9.8-11.6	700	v, composites, satellite	Mota 1997
3-6	-	-	850-500	v, sounding	Coutinho 2007
3-9	2000-4000	6-12	700	Spectral analysis, v, composites,	Diedhiou et al. 2010
5	4000	10	850 and 700	v, satellite, sounding	Torres 2011
5,3	4307	9.5	1000–200	u, v, w, composites, synoptic analysis	Pontes da Silva 2011
5,5	4500	9.5	1000–200	u, v, w, composites, Track	Gomes et al. 2015
4–6	4500	9.5	1000–200	u, v, w, composites, Track	Gomes et al. 2019

Correspondence author: Lucas C. V. Cavalcante email: lucasxave@hotmail.com

Table 2

Research Centers/Groups	Institute (ID)	Model (Spatial Resolution latitude x longitude)
	CMIP (historical)	
Research Center for Environmental Changes	AS-RCEC	TaiESM1 (0.94° x 1.25°)
Beijing Climate Center, China Meteorological Administration	BCC	BCC-CSM2-MR (1.1° × 1.1°)
Chinese Academy of Sciences	CAS	FGOALS-f3-L (1° × 1.25°)
Centro Euro-Mediterraneo per I Cambiamenti Climatici	CMCC	CM2-SR5 (0.94° × 1.25°) CM2-HR4 (0.94° x 1.25°)
EC-EARTH consortium	EC-EARTH	EC-Earth3 (0.7° × 0.7°) EC-Earth3-Veg (0.7° × 0.7°)
Institute for Numerical Mathematics	INM	INM-CM4-8 (1.5° × 2°) INM-CM5-0 (1.5° × 2°)
Max Planck Institute for Meteorology	MPI-M	MPI-ESM1-2-HR (0.9° × 0.9°)
Meteorological Research Institute	MRI	MRI-ESM2-0 (1.1° × 1.1°)
Norwegian Climate Centre	NCC	NorESM2-MM (0.9° × 1.3°)
National Center for Atmospheric Research	NCAR	CESM2 (0.95° × 1.25°) CESM2-WACCM (0.95° × 1.25°) CESM2-WACCM-FV2 (1.95° x 2.5°)
National Oceanic and Atmospheric Administration (NOAA) Geophysical Fluid Dynamics Laboratory	NOAA GFDL	GFDL-CM4 GFDL-ESM4 (1° × 1°)
Seoul National University	SNU	SAM0-UNICON (0.9° × 1.3°)
	AMIP	
Research Center for Environmental Changes	AS-RCEC	TaiESM1 (0.94° x 1.25°)
Chinese Academy of Meteorological Sciences	CAMS	CAMS-CSM1-0 (1.1° × 1.1°)
Chinese Academy of Sciences	CAS	FGOALS-f3-L (1° × 1.25°)
Centro Euro-Mediterraneo per I Cambiamenti Climatici	CMCC	CM2-SR5 (0.94° × 1.25°)
EC-EARTH consortium	EC-EARTH	EC-Earth3 (0.7° × 0.7°) EC-Earth3-Veg (0.7° × 0.7°) EC-Earth3-AerChem (0.7° x 0.7°) EC-Earth3-CC (0.7° × 0.7°)
Institute for Numerical Mathematics	INM	INM-CM4-8 (1.5° × 2°) INM-CM5-0 (1.5° × 2°)
Max Planck Institute for Meteorology	MPI-M	MPI-ESM1-2-HR (0.93° × 0.93°)
National Center for Atmospheric Research	NCAR	CESM2 (0.95° × 1.25°) CESM2-WACCM (0.95° × 1.25°) CESM2-WACCM-FV2 (1.95° x 2.5°)
National Oceanic and Atmospheric Administration (NOAA) Geophysical Fluid Dynamics Laboratory	NOAA GFDL	GFDL-CM4 (1° × 1°) GFDL-ESM4 (1° × 1°)
	hist-1950	
European Centre for Medium-Range Weather Forecasts	ECMWF	ECMWF-IFS-HR (0.50° x 0.50°)
Centro Euro-Mediterraneo per I Cambiamenti Climatici	CMCC	CM2-VHR4 (0.23° x 0.31°)
Research Center for Environmental Changes	AS-RCEC	HiRAM-SIT-LR (0.5° x 0.5°)
Chinese Academy of Sciences	CAS	FGOALS-f3-H (0.25° x 0.25°)

Correspondence author: Lucas C. V. Cavalcante email: lucasxave@hotmail.com

Beijing Climate Center, China Meteorological Administration	BCC	BCC-CSM2-HR (0.45° × 0.45°)
Max Planck Institute for Meteorology	MPI-M	MPI-ESM1-2-XR (0.47° × 0.47°)
Met Office Hadley Centre	MOHC	HadGEM3-GC31-HM (0.23° × 0.35°)
	highresSST-present	
European Centre for Medium-Range Weather Forecasts	ECMWF	ECMWF-IFS-HR (0.50 °x 0.50°) ECMWF-IFS-LR (1.0° × 1.0°)
Institut Pierre-Simon Laplace	IPSL	IPSL-CM6A-ATM-HR (0.50° x 0.70°)
Japan Agency for Marine-Earth Science and Technology, Atmosphere and Ocean Research Institute (The University of Tokyo), and National Institute for Environmental Studies	MIROC	NICAM16-8S (0.28° × 0.28°)
Max Planck Institute for Meteorology	MPI-M	MPI-ESM1-2-XR (0.47° × 0.47°)
Centro Euro-Mediterraneo per I Cambiamenti Climatici	CMCC	CM2-VHR4 (0. 31° x 0.23°)
Research Center for Environmental Changes	AS-RCEC	HiRAM-SIT-LR (0.56° x 0.70°)
Chinese Academy of Meteorological Sciences	CAMS	CAMS-CSM1-0 (0.46° × 0.46°)
Met Office Hadley Centre	MOHC	HadGEM3-GC31-HM (0.23° × 0.35°)
Meteorological Research Institute	MRI	MRI-AGCM3-2H (0.56° × 0.56°)

Table 3

MODEL	TSS	RMSE_A (mm day⁻¹)	RMSE_S (mm day⁻¹)	BIAS_A (mm day⁻¹)	BIAS_S (mm day⁻¹)	R^2	DV_norm (mm day⁻¹)
CMIP							
AS-RCEC.TaiESM1	0.545	2.269	2.474	1.323	2.019	0.734	1.790
CAS.FGOALS-f3-L	0.551	2.338	2.715	1.245	2.873	0.539	1.293
NCC.NorESM2-MM	0.619	1.606	1.664	0.719	3.563	0.666	1.263
AMIP							
CAS.FGOALS-f3-L	0.800	1.094	1.166	0.667	2.740	0.873	0.980
AS-RCEC.TaiESM1	0.859	1.158	1.147	0.761	2.929	0.894	1.134
CMCC-CM2-SR5	0.837	1.239	1.362	0.934	2.849	0.910	1.184
hist-1950							
CMCC-CM2-VHR4	0.648	1.552	1.160	0.095	-0.345	0.710	2.095
ECMWF-IFS-HR	0.718	1.535	1.578	0.748	0.776	0.792	2.182
HadGEM3-GC31-HH	0.852	0.852	0.687	-0.028	0.036	0.905	1.871
highresSST-present							
MRI-AGCM3-2-H	0.873	0.810	0.667	0.381	0.285	0.894	1.178
CMCC-CM2-VHR4	0.881	0.964	0.917	0.572	0.508	0.918	0.954
ECMWF-IFS-HR	0.920	0.815	0.866	0.490	0.563	0.943	1.100

Correspondence author: Lucas C. V. Cavalcante email: lucasxave@hotmail.com

Table 4

MODELS	Mean phase speed (m/s)	Mean lifetime (day)	Mean frequency (EWD/year)	R^2 (ERA5)	R^2 (Gomes et al, 2019)
			CMIP		
NCC.NorESM2-MM	6.65	6.51	31.1	-0.05	-0.05
AS-RCEC.TaiESM1	6.37	6.31	47.6	-0.10	-0.10
			AMIP		
CMCC-CM2-SR5	6.62	6.42	49.5	0.01	0.01
AS-RCEC.TaiESM1	7.07	5.83	46.1	0.35	0.35
			hist-1950		
CMCC-CM2-VHR4	6.90	6.12	64.5	0.23	0.23
ECMWF-IFS-HR	6.94	6.68	75.0	0.06	0.06
			highresSST-present		
CMCC-CM2-VHR4	6.7	5.84	74.7	-0.31	-0.31
ECMWF-IFS-HR	7.07	5.99	78.6	0.34	0.34
ERA5	7.29	5.78	27.7		
Gomes et al (2019)	9.5	5	25		

Correspondence author: Lucas C. V. Cavalcante email: lucasxave@hotmail.com